The Intersection Between the Oculomotor Nerve and the Internal Carotid Artery to Distinguish Extracavernous and Intracavernous Paraclinoid Aneurysms Using Anatomic Dissections—A New 3T Magnetic Resonance Imaging Protocol Confirmed by Three-Dimensionally Printed Biomodels

Hugo Leonardo Doria-Netto[1,2], Christiane Monteiro de Siqueira Campos[3], Victor Hugo Rocha Marussi[3], José Maria Campos-Filho[1,2], Jean Faber[1], Michael T. Lawton[4], Feres E.A. Chaddad-Neto[1,2]

■ OBJECTIVE: **To evaluate the relationship between the oculomotor nerve (CNIII) and the internal carotid artery (ICA) as a new anatomic-radiologic landmark for distinguishing the exact location of a paraclinoid intracranial aneurysm (IA).**

■ METHODS: **Microanatomic dissections were performed in 20 cavernous sinuses to evaluate the ICA paraclinoid region. Based on anatomic observations, a new magnetic resonance (MRI) protocol to classify paraclinoid aneurysms was proposed. MRI of 42 IAs from 34 patients was independently analyzed and classified as intracavernous, extracavernous, or transitional by 2 neuroradiologists. To validate the proposed MRI protocol, each IA was classified by a three-dimensionally (3D) printed biomodel and agreement with the radiologic classifications was evaluated. Of 42 IAs, 23 undergoing microsurgeries were also classified by direct visualization.**

■ RESULTS: **We observed that the true cavernous sinus roof is defined by the carotid-oculomotor membrane, which has an intimate relationship with the intersection between the superior limit of the CNIII and the ICA. Based on this intersection, all 42 IAs were radiologically classified and agreement with the 3D printed biomodels was observed in 95% IAs. Concordance tests showed a statistically significant ($P < 0.05$) agreement between the classifications. All 23 IAs treated had the radiologic and 3D biomodel classification confirmed.**

■ CONCLUSIONS: **The intersection between the ICA and the CNIII, which crosses it transversely in its entire diameter, is a reliable anatomic-radiologic landmark to correctly classify paraclinoid aneurysms. Through a new MRI protocol, it is possible to radiologically identify this intersection and to easily distinguish the intracavernous and extracavernous ICA paraclinoid aneurysms.**

INTRODUCTION

The presence of an intracranial aneurysm (IA) above the limit of the cavernous sinus (CS) (extracavernous) on the internal carotid artery (ICA) creates risk for subarachnoid hemorrhage (SAH) and usually requires treatment, whereas aneurysms located entirely within the CS (intracavernous) have a

Key words
- 3D printed biomodels
- Anatomic landmarks
- Internal carotid artery
- Intracranial aneurysm
- Magnetic resonance imaging
- Oculomotor nerve
- Paraclinoid aneurysm

Abbreviations and Acronyms
3D: Three-dimensional
ACP: Anterior clinoid process
CC: Carotid cave
CI: Confidence interval
CNIII: Cranial nerve III (oculomotor nerve)
COM: Carotid-oculomotor membrane
CS: Cavernous sinus
CT: Computed tomography
DDR: Distal dural ring
FIESTA: Fast imaging employing steady-state acquisition
FOV: Field of view
IA: Intracranial aneurysm
ICA: Internal carotid artery
MRA: Magnetic resonance angiography
MRI: Magnetic resonance imaging
OA: Ophthalmic artery
PDR: Proximal dural ring
SAH: Subarachnoid hemorrhage
SPACE: Sampling perfection with application-optimized contrasts using different flip angle evolution
TOF: Time of flight

From the [1]Department of Neurology and Neurosurgery, Universidade Federal de São Paulo (Unifesp), São Paulo, São Paulo, Brazil; Divisions of [2]Neurosurgery and [3]Neuroradiology, Hospital Beneficência Portuguesa de São Paulo, São Paulo, Brazil; and [4]Department of Neurological Surgery, Barrow Neurological Institute, St. Joseph's Hospital and Medical Center, Phoenix, Arizona, USA

To whom correspondence should be addressed: Feres E. A. Chaddad-Neto, M.D., Ph.D. [E-mail: feres.chaddad@unifesp.br]

Citation: World Neurosurg. (2022) 167:e475-e506.
https://doi.org/10.1016/j.wneu.2022.08.030

*Journal homepage: **www.journals.elsevier.com/world-neurosurgery***

*Available online: **www.sciencedirect.com***

negligible risk of SAH and lower morbidity compared with extracavernous paraclinoid IAs.[1-7] The only reliable method used to certify whether the paraclinoid aneurysms is intracavernous or extracavernous is the direct microsurgical view. For a rational diagnostic and selection of the best treatment option, it is essential to determine the exact location of the paraclinoid aneurysms. However, compared with other sites of anterior circulation aneurysms, the paraclinoid region of the carotid artery has a complex anatomy.[5,8-10]

Among the proposals for identifying the location of paraclinoid aneurysms are, for example, the establishment of the relationship between the anterior clinoid process (ACP) and the IA,[11] the relationship between the ophthalmic artery (OA)[12] or the optic struct[13,14] and the aneurysmal neck, and the attempt to identify relationships with the distal dural ring (DDR) on magnetic resonance imaging (MRI)[15-17] and computed tomography (CT) angiography.[18] However, there is weakness in these proposals, which have a poor sample, or lack of a strong statistical analysis, which raises the possibility of some structures being mistakenly used as landmarks.

In anatomic studies,[7,19] the roof of the CS was found to be determined by a tenuous connective membrane, the carotid-oculomotor membrane (COM), also called proximal dural ring (PDR), which has a close relationship with the intersection between the ICA and the oculomotor nerve, also called the third cranial nerve (CNIII), which crosses it transversally throughout its length.[20-22] If radiologically identified, this intersection can be an anatomic-radiologic landmark, faithfully correlated to the COM/PDR, for the exact distinction between the cavernous segment of the ICA and its other segments. Therefore, this study aimed to analyze the relationship between the CNIII and the ICA as a new clinical anatomic-radiologic landmark for the exact location of a paraclinoid aneurysm.

METHODS

Study Design and Population

This investigation was performed in 4 stages: anatomic, radiologic, three-dimensional (3D) biomodel printing, and surgical. In the prospective anatomic stage, 10 cadaverous specimens (20 cerebral hemispheres) were dissected. For clinical stages, medical records, medical images, 3D-printed biomodels of 34 patients (42 aneurysms) and neurosurgical videos of 20 patients (23 aneurysms) were prospective evaluated (Figure 1). The study was approved by the research ethics committees of Hospital São Paulo-UNIFESP (number 3.116.206) and Hospital Beneficência Portuguesa of São Paulo (number 4.753.949). The need for informed consent was waived by both ethics committees.

Clinical stages included review of patients' data with IA, ruptured or not, supposedly located in the distal cavernous, clinoid, carotid cave (CC), or ophthalmic ICA segments, treated at Hospital São Paulo and at Hospital Beneficência Portuguesa of São Paulo, collected from September 2018 to April 2020. Patients with incomplete or low-quality imaging tests were excluded.

Anatomic Stage

Dissections were performed on 20 silicone dye–injected fresh cadaveric cerebral hemispheres to determine the ICA paraclinoid segments comparing them in relation to the CNIII, the PDR or COM, and DDR. The microanatomic dissection procedure was performed by pterional craniotomy and transylvian access, exposing fundamental structures. Then, an anterior clinoidectomy was performed, followed by the incision of the optic nerve sheath and resection of the falciform ligament over the optic nerve.[23-25] Afterward, the DDR was opened, and the analysis of the COM was performed in close relationship with the ICA and its intersection with CNIII. The distances between the COM and DDR, measured on the superior and inferior walls of the ICA and the distance between CNIII and the ICA, were also analyzed along with the entire intersection between these anatomic structures. The analysis of the presence or absence of the CC was also performed, as well as the characteristics of the OA, CS, and carotid collar.

Radiologic Stage

The radiologic stage involved analysis of MRI and magnetic resonance angiography (MRA) examination of 34 patients performed in 3T (Siemens-Skyra Evolve, Erlangen, Germany) and GE (GE Healthcare, HDXT, Milwaukee, Wisconsin, USA) equipment. CT without intravenous contrast was used to acquire bone images for 3D biomodel printing.

MRI Protocol. High-resolution images were acquired, following the established protocol, in two-dimensional coronal T2 fast spin echo sequences with thickness of 2.0 mm × 0 matrix of 384/384, field of view (FOV) of 20 × 20, voxel of 0.4 × 0.4 × 2.0 mm, time 4 minutes 30 seconds; in coronal fast imaging employing steady-state acquisition (FIESTA)/sampling perfection with application-optimized contrasts using different flip angle evolution (SPACE) thickness of 0.8 mm, matrix of 320 × 256, FOV 20 × 20, voxel of 0.3 × 0.3 × 0.8 mm, time of 4 minutes 30 seconds; intracranial arterial MRA in 3D time of flight (TOF) technique with and without gadolinium, for vascular analysis, 0.75 mm thick, 384 × 256 matrix, 18 × 18 FOV, 0.2 × 0.2 × 0.8 voxel mm, time of 6 minutes 50 seconds. In addition to the sequences initially performed (coronal T2, coronal FIESTA, and 3D TOF), sagittal T1 sequence isotropic volumetric pregadolinium and postgadolinium was added (SPACE/spectral attenuated inversion recovery, and Cube [GE Healthcare]) with 0.9 mm thick, matrix 288 × 288, FOV 23 × 23, time 6 minutes 14 seconds, echo time 16 and repetition time 600. Volumetric sequences of CS were also performed, postcontrast, with 0.1 mm thick, 450/450 matrix, 18 × 18 FOV, time of 3 minutes 31 seconds. The intersection between the ICA and CNIII was identified in the sequences coronal T2/Coronal FIESTA/T1 volumetric with intravenous contrast and axial 3D TOF postgadolinium (Figure 2).

Radiologic Classification. The radiologic results were evaluated and classified, blindly and independently, by 2 neuroradiologists. Paraclinoid aneurysms were classified according to its relationship with the intersection between the ICA and CNIII (ICA × CNIII) as follows:

- Superior or extracavernous: IA located above the superior limit of CNIII, with the aneurysm neck and dome distal to ICA × CNIII;
- Transitional: IA located at the level of the superior limit of CNIII, with part of the aneurysm neck or dome located

superiorly and part located inferiorly to the superior limit of the ICA × CNIII;

- Inferior or intracavernous: IA located below the superior limit of CNIII, with the aneurysm neck and dome located below the ICA × CNIII, within the CS.

3D Biomodel Printing Stage

The 3D biomodel was prospectively printed using images of each aneurysm acquired from different 3T MRI/MRA through the fusion of sequences suitable for constructing each anatomic structure. Each biomodel was segmented with Brainlab Elements software

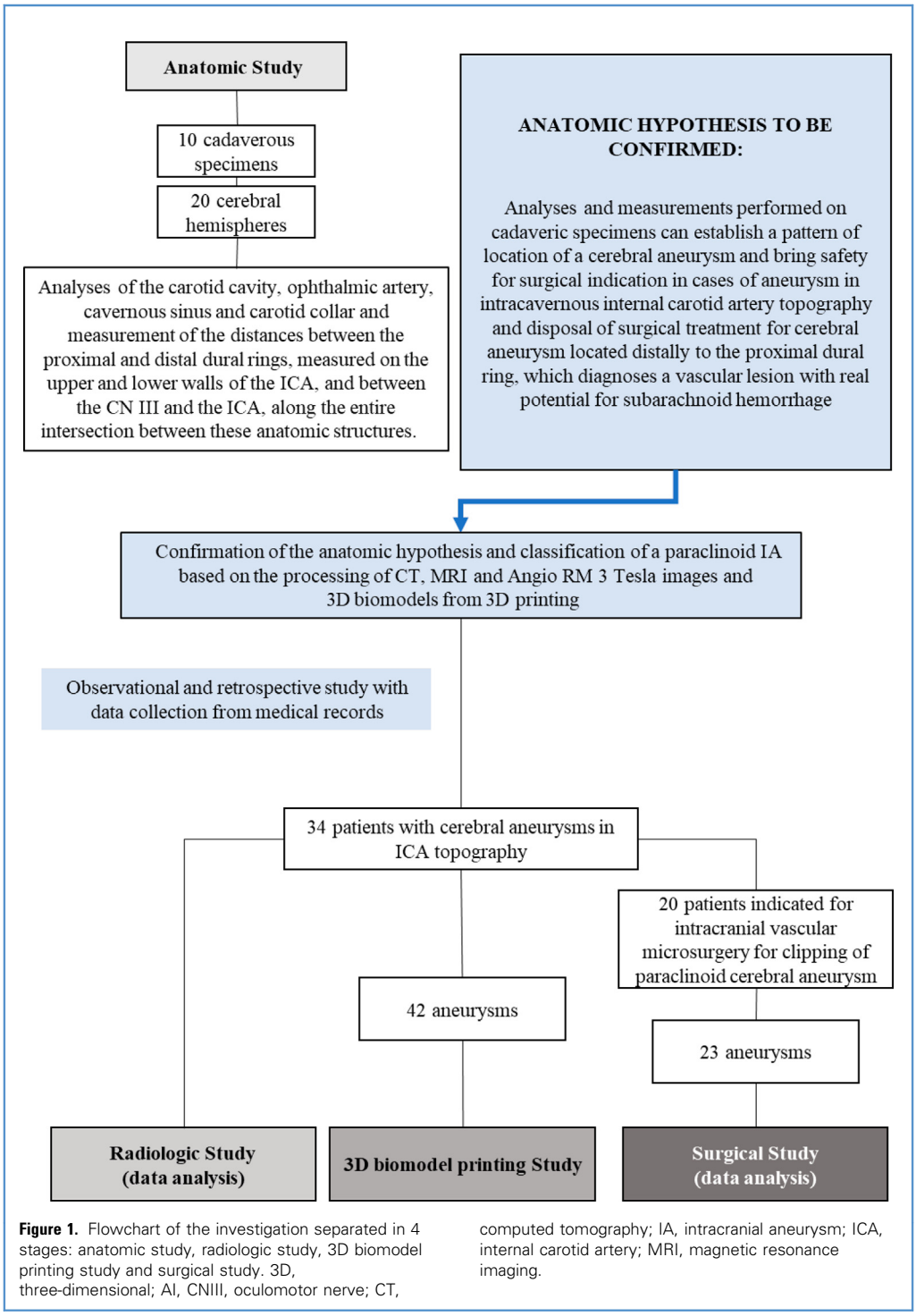

Figure 1. Flowchart of the investigation separated in 4 stages: anatomic study, radiologic study, 3D biomodel printing study and surgical study. 3D, three-dimensional; AI, CNIII, oculomotor nerve; CT, computed tomography; IA, intracranial aneurysm; ICA, internal carotid artery; MRI, magnetic resonance imaging.

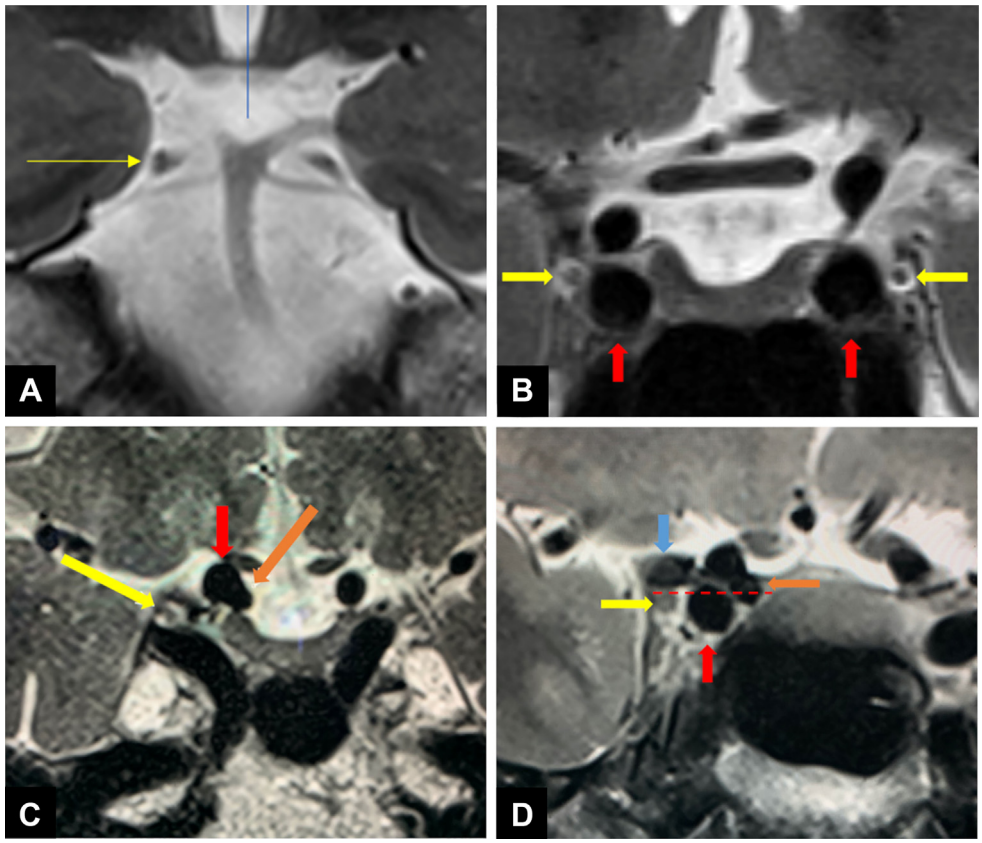

Figure 2. Magnetic resonance imaging (MRI) evaluated by neuroradiologists. (**A**) Bilateral identification of CNIII (oculomotor nerve) (*yellow arrow*) on 3T T2 MRI, coronal sections showing that both CNIIIs are contained in the interpeduncular cistern between the posterior cerebral artery, superiorly, and the superior cerebellar artery, inferiorly. (**B**) Location of CNIII (*yellow arrows*) and internal carotid artery (ICA) (*red arrows*) left and right, on 3T MRI T2 sequence, coronal thin sections. (**C**) Location of CNIII (*yellow arrow*), ICA (*red arrow*), and left intracranial aneurysm (*orange arrow*) on 3T MRI in fast imaging employing steady-state acquisition sequence, axial section. In (**B**) and (**C**), emphasis on the cerebrospinal fluid cistern adjacent to the CNIII, showing a hypersignal halo provided by the cerebrospinal fluid, surrounding the CNIII on the verge of its entry into the posterior roof of the cavernous sinus, in the topography of the CNIII trigone. (**D**) Identification of CNIII (*yellow arrow*) at its intersection with the paraclinoid ICA (*red arrow*) in the cavernous sinus. The anterior clinoid process (*blue arrow*) can be seen just above the CNIII. The *dashed line* connecting the superior limit of the CNIII, laterally, to the ICA, medially, is used to assess and classify the IA under study, classified as superior or extracavernous in this image, the entire aneurysm neck being above the superior limit of the CNIII.

(Brainlab, Munich, Germany), in which we fused the MRI-specific sequences for identification of each anatomic structure.

Vascular reconstruction was extracted from 3D TOF intracranial MRA, axial T1 TOF was used to identify ICA and IA, and CNIII in all its extension was identified from the FIESTA volumetric and coronal T2 fast spin echo sequences. In its path within the CS, CNIII was identified by fusing images from the coronal T2 sequence with fine cuts in high resolution or volumetric coronal FIESTA and a specific sequence for the CS as the T1-weighted volumetric isotropic sequence (SPACE/spectral attenuated inversion recovery, or Cube) (**Figure 3**).

Each biomodel, as shown in **Figure 4**, was modeled by Mimics software (Materialise NV, Leuven, Belgium) and printed by Stratasys J750 printer (Stratasys Ltd., Eden Prairie, Minnesota, USA). The IAs printed in 3D were classified by the neurosurgeon as superior, inferior, or transitional, comparing their necks with the superior limit of CNIII.

Surgical Stage

For treatment indication, patients were judged by neurosurgeons and neuroradiologists. Of the 34 patients, 20 patients with 23 paraclinoid IAs underwent microsurgical treatment,[23-25] as described in **Appendix A**. Neurosurgical videos of all patients were collected and then analyzed to confirm or deny the anatomic and radiologic hypotheses.

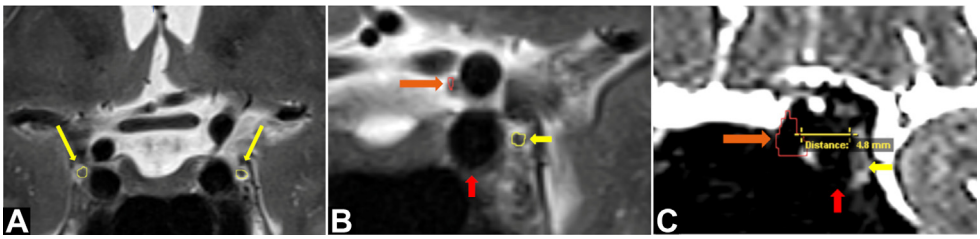

Figure 3. Magnetic resonance imaging (MRI) used for fusion of radiologic sequences. (**A**) 3T MRI in coronal T2 sequence for identification of CNIII (oculomotor nerve) (*yellow arrows*) bilaterally. Both CNIIIs were better highlighted and segmented from the coronal T2 and fast imaging employing steady-state acquisition (FIESTA) sequence. (**B**) 3T MRI in T2 coronal sequence and (**C**) 3T MRI in FIESTA coronal sequence, segmented using software for image fusion. In (**B**) and (**C**), CNIII (*yellow arrow*) and intracranial aneurysm (IA) (*orange arrow*) had their images originally obtained from FIESTA and T1 time of flight, respectively. The *red arrow* indicates the location of the internal carotid artery (ICA) originally also obtained from the T1 time of flight sequence, which is the best sequence for accurate identification of IA and ICA. It is possible to observe the line drawn connecting the superior limit of CNIII (*yellow arrow*), laterally, to the ICA (*red arrow*), medially, which is used for the assessment and classification of the IA under investigation, in this case, classified as superior or extracavernous. There is a distance (4.8 mm) measured between CNIII and IA.

Statistical Analysis

Variables such as age, sex, aneurysm size, ICA wall affected by the aneurysm, and distance between CNIII and ICA were reported by absolute and relative frequencies. The compatibility between the classifications of the 2 independent neuroradiologists and the 3D biomodel was evaluated and described by absolute frequencies. To exclude randomness in the analysis of agreement between classifications, surrogate data were generated by randomly shuffling the 3D biomodel classification. Statistical analyzes were performed using MATLAB version 16b (MathWorks, Natick, Massachusetts, USA) using the statistics toolbox together with the implementation of its own algorithms.

RESULTS

In the anatomic stage, we observed the COM, or the PDR, as a connective tissue membrane connected to the superior limit of CNIII, laterally, and the ICA, medially, as a line that crosses the entire diameter of the ICA transversely in the exact location of the COM. This intersection defines the real roof of the CS in the

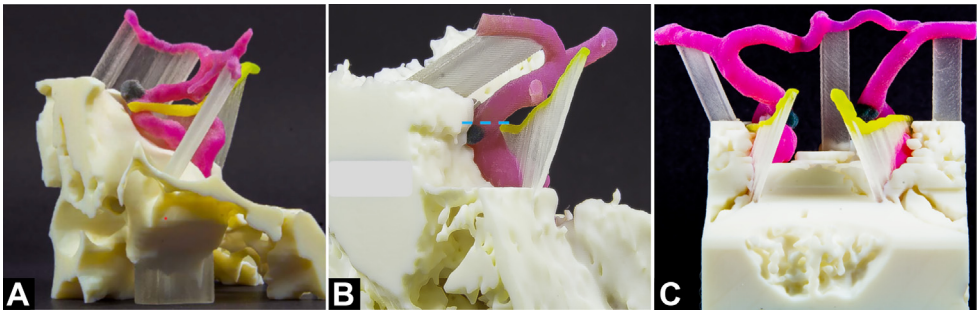

Figure 4. Three-dimensional (3D) biomodel made from radiologic images of patients. 3D-printed biomodels showing the intracranial aneurysms (IAs) were printed in *black* and its relationship with the superior limit of CNIII (oculomotor nerve) in *yellow* at its intersection with the internal carotid artery (ICA) in *pink*. In transparent acrylic, the supports for the anatomic structures in their exact anatomic positions were printed after 3D printing. For IA classification in 3D biomodels, a line (*blue dashed line*) was drawn between the superior limit of CNIII, laterally, and the ICA, medially, which was used as the parameter compared with the aneurysmal necks for IA classification as superior, inferior, or transitional. (**A**) IA classified as extracavernous or superior to the superior limit of CNIII at its intersection with the ICA. (**B**) IA classified as intracavernous or inferior the superior limit of CNIII (*yellow*) at its intersection with the ICA (*pink*), on a 3D-printed biomodel. (**C**) Bilateral IAs classified as extracavernous or superior the superior limit of CNIII at its intersection with the ICA. On the left side, the IA is located on the medial ICA wall. On the right side, the IA is located on the inferior ICA wall.

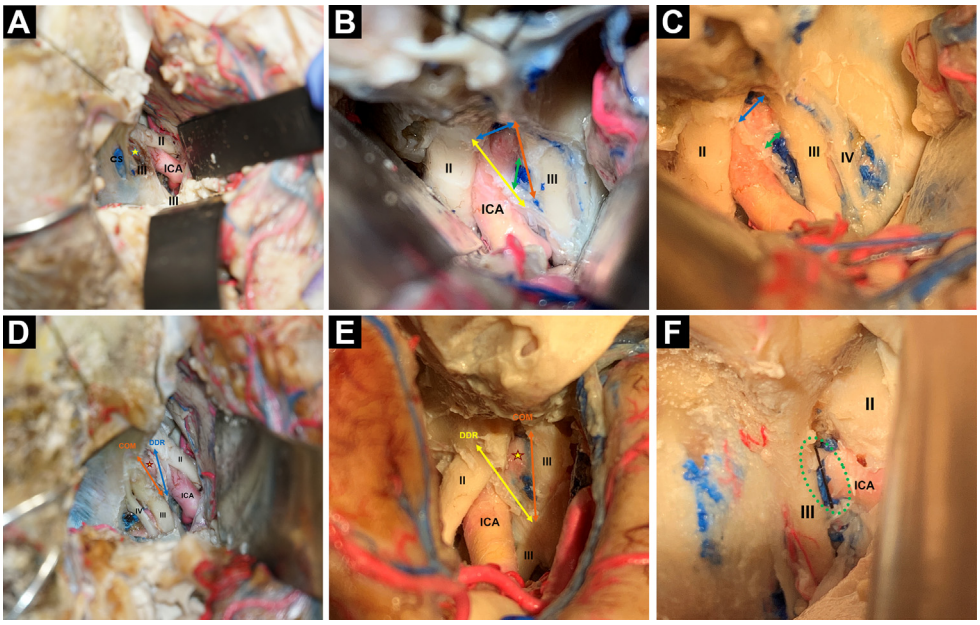

Figure 5. Cadaveric dissections. (**A**) Representative image of cadaveric dissections after anterior clinoidectomy with evidence of distal dural ring (DDR) and carotid-oculomotor membrane (COM), not dissected, internal carotid artery (ICA) in C5 (*yellow star*) and C6, cranial nerves II (or optic nerve) and III (or oculomotor nerve) and CS (cavernous sinus) exposed on purpose after fenestration of its lateral wall. (**B**) and (**C**) Distance between the distal and PDRs measured on the superior or anterior wall of the clinoidal ICA (*blue arrow*) and on the inferior or posterior wall of the clinoidal ICA (*green arrow*) showing the diagonal pattern of the dural rings in addition to their proximity in the posterior or inferior wall of the ICA, an anatomic feature that makes it difficult to exactly locate the intracranial aneurysm (IA) on the posterior or inferior wall of the paraclinoid ICA. (**D**) and (**E**) COM, DDR, and ICA clinoid segment (C5) (*red star*). Emphasis on the intersection between the COM and the ICA, in which there is the crossing of the entire diameter of the ICA by the CNIII (oculomotor nerve), because its superior edge delimits the real roof of the cavernous sinus and, therefore, precisely distinguishes the cavernous ICA, inferiorly to the superior limit of the CNIII, from the clinoid ICA, superiorly to the superior limit of the CNIII, through the identification of this intersection. (**F**) Presence of the carotid collar, with evidence of pericavernous venous plexus rising just above the COM, without, however, being part of the cavernous sinus. Virtual distance between the CNIII (laterally) and the paraclinoid ICA (medially), crossed in its entire diameter by the CNIII. Emphasis on black 4.0 nylon suture (*green circle*) photographed exactly at COM, highlighting the real superior limit of the cavernous sinus. II, optic nerve; IV, trochlear nerve.

paraclinoid ICA, distinguishing the cavernous from the clinoid ICA, which can be established as an anatomic landmark for the exact identification of a paraclinoid aneurysm (Figure 5).

In addition, we found different distances between the DDR and the PDR measured on the superior and inferior wall of the ICA, proving the extreme proximity between these structures on the inferior or posterior wall of the ICA (Figure 5B and C and Appendix B).

Based on the anatomic hypothesis, we proposed a new MRI protocol through a radiologic evaluation of 34 patients with 42 paraclinoid aneurysms. Six patients (17.6%) had multiple aneurysms, and 54.76% of IAs were found in the right paraclinoid ICA. Regarding orientation, 33 IAs (78.6%) were located on the medial and inferior/posterior ICA walls (orientation I), and 9 (21.4%) were on the superior/anterior and lateral ICA walls (orientation II) (Table 1). The neuroradiologists independently classified all 42 aneurysms according to their relationship between the aneurysmal neck and the intersection between the superior limit of CNIII and the ICA as superior, transitional, or inferior. Total agreement between the neuroradiologists was obtained in 38/42 IAs (90.5%) (Table 2). In 3 of the 4 incompatible cases (9.5%), the aneurysm size were 2–2.5 mm. In addition, in 1 case of an IA of 2.5 mm, there was an anatomic variation related to an Asian patient, which may explain the case with the greatest distance between the CNIII and the ICA (2.6 mm), which was unique in this study. This greater distance tends to make it difficult to assess the relationship among the ICA, aneurysmal neck, and CNIII. To confirm the radiologic classifications, all 42 IAs were printed in 3D biomodels with complete reliability to the patient's anatomy. The ICA segments and anatomic structures in the 3D biomodel are described in Figure 6.

Because of its total accuracy and anatomic reliability, the 3D biomodel was considered the parameter in the classification of IAs as superior, inferior, or transitional (Table 2 and Figure 7). The 3D biomodels were evaluated and 26/42 (61.9%) IAs were classified as

Table 1. Characteristics of Patients and the Studied Paraclinoid Aneurysms of Patients

Patient Number	Patient's Age (years)	Patient's Sex	Number of Aneurysms	Aneurysm Orientation	Aneurysm Brain Side	Aneurysm Size (mm)
1	49	F	1	I	L	4
2	77	F	1	I	R	4
3	38	F	1	I	R	4
4	61	F	1	I	L	4
5	50	F	1	I	R	4
6	52	F	1	I	R	4
7	56	F	2	I	R/bilateral	4
				I	L/bilateral	4
8	69	F	1	II	L	3
9	43	F	1	I	R	4
10	44	F	1	I	L	5
11	64	F	1	I	R	2
12	56	F	1	I	R	3
13	58	F	1	I	R	3
14	36	F	1	I	L	7
15	59	F	2	II	R	6
				I	R	6
16	42	F	1	I	R	3
17	69	F	1	I	R	2
18	39	F	1	I	L	4
19	45	F	3	I	R/bilateral	1.5
				I	R/bilateral	3
				I	L/bilateral	5
20	45	F	2	II	R/bilateral	2
				II	L/bilateral	2
21	53	F	2	I	R/bilateral	2
				I	L/bilateral	3
22	51	F	1	I	L	3
23	48	F	1	I	R	3
24	76	F	1	I	L	3
25	68	F	1	I	L	2.5
26	59	F	1	I	R	3
27	32	F	2	II	R/bilateral	6
				II	L/bilateral	3
28	43	M	1	II	L	5
29	33	F	1	I	L	3
30	56	F	2	II	R/bilateral	3.4
				I	L/bilateral	3.8

F, female; L, left; R, right; M, male.

Continues

Table 1. Continued

Patient Number	Patient's Age (years)	Patient's Sex	Number of Aneurysms	Aneurysm Orientation	Aneurysm Brain Side	Aneurysm Size (mm)
31	62	F	1	I	R	4
32	38	F	1	I	L	5
33	73	F	1	I	L	4
34	56	F	1	II	R	5
Total (N = 34)	52.16	M, 1/F, 41	42	I, 33 [78.6%]; II, 9 [21.4%]	R, 23 [54.76%]; L, 19 [45.23%]; R and L, 6 [17.64%]	3.695
Classification by the three-dimensional biomodel						
Superior	51.88	M, 1/F,25	26	I, 19 [67.86%]; II, 7 [32.14%]	R, 15 [57.7%]; L, 11 [43.3%]	3.99
Inferior	52.4	F, 15	15	I, 13 [86.67%]; II, 2 [13.33%]	R, 7 [46.66%]; L,8 [53.33%]	3.22
Transitional	56	F	1	I, 1 [100%]	R	3

F, female; L, left; R, right; M, male.

Table 2. Classification and Treatment of the Studied Paraclinoid Aneurysms of Patients

Patient Number	Radiologic Classification of Aneurysm		Classification by the 3D Biomodel	Radiologic Classification Compatibility with the 3D Biomodel	Microsurgical Treatment by Clipping
	Radiologist 1	Radiologist 2			
1	INF	INF	INF	Yes	No
2	SUP	SUP	SUP	Yes	Yes
3	INF	INF	INF	Yes	No
4	SUP	SUP	SUP	Yes	Yes
5	**INF**	**SUP**	**SUP**	Yes*	No
6	SUP	SUP	SUP	Yes	Yes
7	R: SUP	R: SUP	SUP	Yes	No
	L: INF	L: INF	INF	Yes	Yes
8	SUP	SUP	SUP	Yes	Yes
9	SUP	SUP	SUP	Yes	Yes
10	INF	INF	INF	Yes	No
11	INF	INF	SUP	No	No
12	TRANS	TRANS	TRANS	Yes	No
13	SUP	SUP	SUP	Yes	Yes
14	SUP	SUP	SUP	Yes	Yes
15	SUP	SUP	SUP	Yes	Yes
	SUP	SUP	SUP	Yes	Yes
16	SUP	SUP	INF	No	No
17	**SUP**	**INF**	**INF**	Yes*	No
18	SUP	SUP	SUP	Yes	Yes

Continues

Table 2. Continued

Patient Number	Radiologic Classification of Aneurysm		Classification by the 3D Biomodel	Radiologic Classification Compatibility with the 3D Biomodel	Microsurgical Treatment by Clipping
	Radiologist 1	Radiologist 2			
19	R: SUP	R: SUP	SUP	Yes	Yes
	R: SUP	R: SUP	SUP	Yes	Yes
	L: SUP	L: SUP	SUP	Yes	Yes
20	R:SUP	R:SUP	SUP	Yes	Yes
	L: TRANS	**L: INF**	**INF**	Yes*	No
21	R: INF	R: INF	INF	Yes	No
	L: INF	L: INF	INF	Yes	No
22	INF	INF	INF	Yes	No
23	SUP	SUP	SUP	Yes	Yes
24	INF	INF	INF	Yes	No
25	**INF**	**SUP**	**SUP**	Yes*	No
26	INF	INF	INF	Yes	No
27	R: SUP	R: SUP	SUP	Yes	Yes
	L: SUP	L: SUP	SUP	Yes	Yes
28	SUP	SUP	SUP	Yes	Yes
29	INF	INF	INF	Yes	No
30	R: INF	R: INF	INF	Yes	No
	L: SUP	L: SUP	SUP	Yes	Yes
31	INF	INF	INF	Yes	No
32	SUP	SUP	SUP	Yes	Yes
33	SUP	SUP	SUP	Yes	Yes
34	SUP	SUP	SUP	Yes	Yes
Total (N = 34)	SUP, 25 [59.5%]; INF: 15 [35.71%]; TRANS: 2 [4.76%]	SUP: 26 [61.9%]; INF: 15 [35.71%]; TRANS: 1 [2.38%]	SUP: 26 [61.9%]; INF: 15 [35.71%]; TRANS: 1 [2.38%]	Yes, 36; Yes#, 4; No 2	Yes, 23 (20 patients); No, 19 (14 patients)
Classification by the 3D biomodel					
SUP	SUP, 23; INF, 3	SUP, 25; INF, 1	SUP	Yes, 23; Yes#, 2; No, 1	Yes, 22; No, 4
INF	SUP, 2; INF, 12; TRANS, 1	SUP, 1; INF, 14	INF	Yes, 12; Yes#, 2; No, 1	Yes, 1; No, 14
TRANS	TRANS	TRANS	TRANS	Yes	No

3D, three-dimensional; INF, inferior; SUP, superior; R, right; L, left; TRANS, transitional.
In bold are non-compatible classifications between both neuroradiologists and 3D biomodel.
*IA classification compatible between one of the neuroradiologists and the 3D biomodel. # Two IA classified as SUP and two other IA as INF were compatible between one of the neuroradiologists and the 3D biomodel.

superior, 15/42 (35.71%) as inferior, and 1/42 (2.38%) as transitional (Table 2). We obtained compatibility of 40 cases (95.23%) between the independent analyses of each neuroradiologist with the biomodel (Table 2), among which 36 cases (90%) were compatible in all 3 evaluations, and 4 (10%) were compatible between the 3D biomodel and one of the neuroradiologists (Table 2).

The 2 IAs considered incompatible were not in agreement with the 3D biomodel, despite the compatibility between both neuroradiologists. In the first case, the neuroradiologists classified the aneurysm as intracavernous, whereas the analysis of the biomodel proved that the aneurysm studied was extracavernous. This case showed an aneurysm in the medial wall topography of the right ICA, with a size of 2 mm and a distance between the CNIII and the

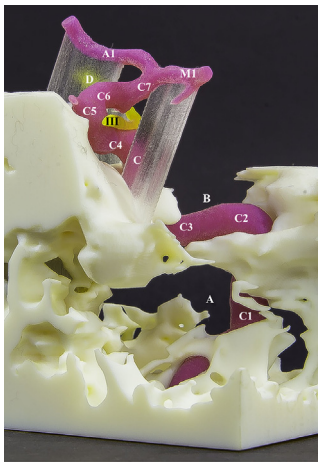

Figure 6. Three-dimensionally printed anatomic biomodel of the internal carotid artery (ICA) segments as the Bouthillier and van Loveren classification (Bouthillier A, van Loveren HR, Keller JT. Segments of the internal carotid artery: a new classification. *Neurosurgery*. 1996;38:425-432 [discussion 432-423]. C1 shows the first ICA segment called cervical. C2 points to the petrous internal carotid artery (ICA) segment. C3 is the lacerous ICA segment. C4 refers to the cavernous ICA segment. C5 is the clinoid ICA segment. C6 is the ophthalmic ICA segment and C7 points to the posterior communicating ICA segment. III points to the oculomotor nerve. According to the Rhoton classification, the ICA is shared into 4 segments designated as cervical (A), petrous (B), cavernous (C), and ophthalmic (D). A1 is the Rhoton anterior cerebral artery first segment, whereas M1 is the first segment of middle cerebral artery on the Rhoton classification.

ICA of 1.6 mm. In the second case, the neuroradiologists classified the aneurysm as extracavernous, whereas the analysis of the biomodel proved that the aneurysm studied was intracavernous. This case showed an aneurysm in the topography of the medial and inferior wall of the right ICA, with a size of 3 mm and a distance between the CNIII and the ICA of 0.4 mm.

The agreements between each neuroradiologist and the 3D biomodel could be the result of random classifications that obtained a good agreement. Therefore, to exclude randomness in the concordance analysis between radiologists 1 and 2 and the 3D biomodel, and to validate the proposed MRI protocol, a mathematical model with surrogate data based on the classification of the 3D biomodel was generated, in which all 42 cases were randomly classified as superior, inferior, or transitional (**Figure 8A** and **B**).

For each aneurysm analyzed individually, the difference between the classification by the surrogate model and the other classifications is notable (**Figure 8C–E**). Between the 2 neuroradiologists, using the odds ratio test and the χ^2 test, the agreement was significant for the 3 classifications of aneurysms ($P < 0.01$). The agreement tests also showed a statistically significant agreement between neuroradiologist 1 and the 3D biomodel ($P < 0.01$) and neuroradiologist 2 and the 3D biomodel ($P < 0.01$) for the 3 classifications of aneurysms. The mathematical model generated a random uniform sequence based on the classification of aneurysms classified by the 3D biomodel and when compared with the classifications of neuroradiologists, there was no agreement with either neuroradiologist 1 ($P > 0.4$) or neuroradiologist 2 ($P > 0.5$) for any of the 3 classifications (**Appendix C**, **Figure C.1**). Other concordance tests (Goodman-Kruskal γ test, κ index, and discordance ratio) also showed a statistically significant ($P < 0.05$) agreement between the classifications obtained between both neuroradiologists and between each neuroradiologist and the 3D biomodel, and no agreement was observed with the surrogate data (**Appendix C**). Therefore, we can exclude randomness as a bias in our study.

Through direct visualization, all 23 aneurysms submitted to microsurgical clipping confirmed the previous radiologic and 3D classification (**Table 2**), indicating that the proposed MRI protocol is reliable. Statistical significance ($P < 0.05$) was also obtained in agreement tests between evaluators for classification of operated and nonoperated aneurysms (**Appendix C**).

In addition, based on a conditional probability relationship, there was a greater tendency to correctly classify aneurysms located in the lateral and superior or anterior wall of the ICA (orientation II) compared with aneurysms located in the medial and inferior or posterior wall of the ICA (orientation I) (**Figure 9**). Among all aneurysms with type I orientation, most were classified as superior, and almost all were operated on (**Figure 9A**). Among all aneurysms with type II orientation, all IAs classified as superior were operated on and therefore surgically proved to be superior (**Figure 9B**).

DISCUSSION

The exact location of a paraclinoid aneurysm is essential for accurate diagnosis, risk management, and therapeutic planning. However, only neurosurgical exploration has so far been able to accurately confirm the location of a paraclinoid aneurysm.[26,27]

There are risks in proposing a treatment without knowing the exact location of the paraclinoid IA. The worst-case scenario is treating a patient with an intracavernous IA (into the cavernous ICA segment [C4]), with reduced risk related to SAH,[28] with microsurgical or endovascular treatment, or not treating an extracavernous IA (into the clinoid segment [C5] or supraclinoid [C6] ICA segments) with increased risk of SAH.[29]

Although several techniques have been proposed for the accurate diagnosis of paraclinoid aneurysm, none has proved to be significantly effective and reliable because they were evaluated in restricted sample case series, on a poor statistical basis, based on mistaken or complicated anatomic repairs, imprecise radiologic examination results, or absent surgical confirmation.

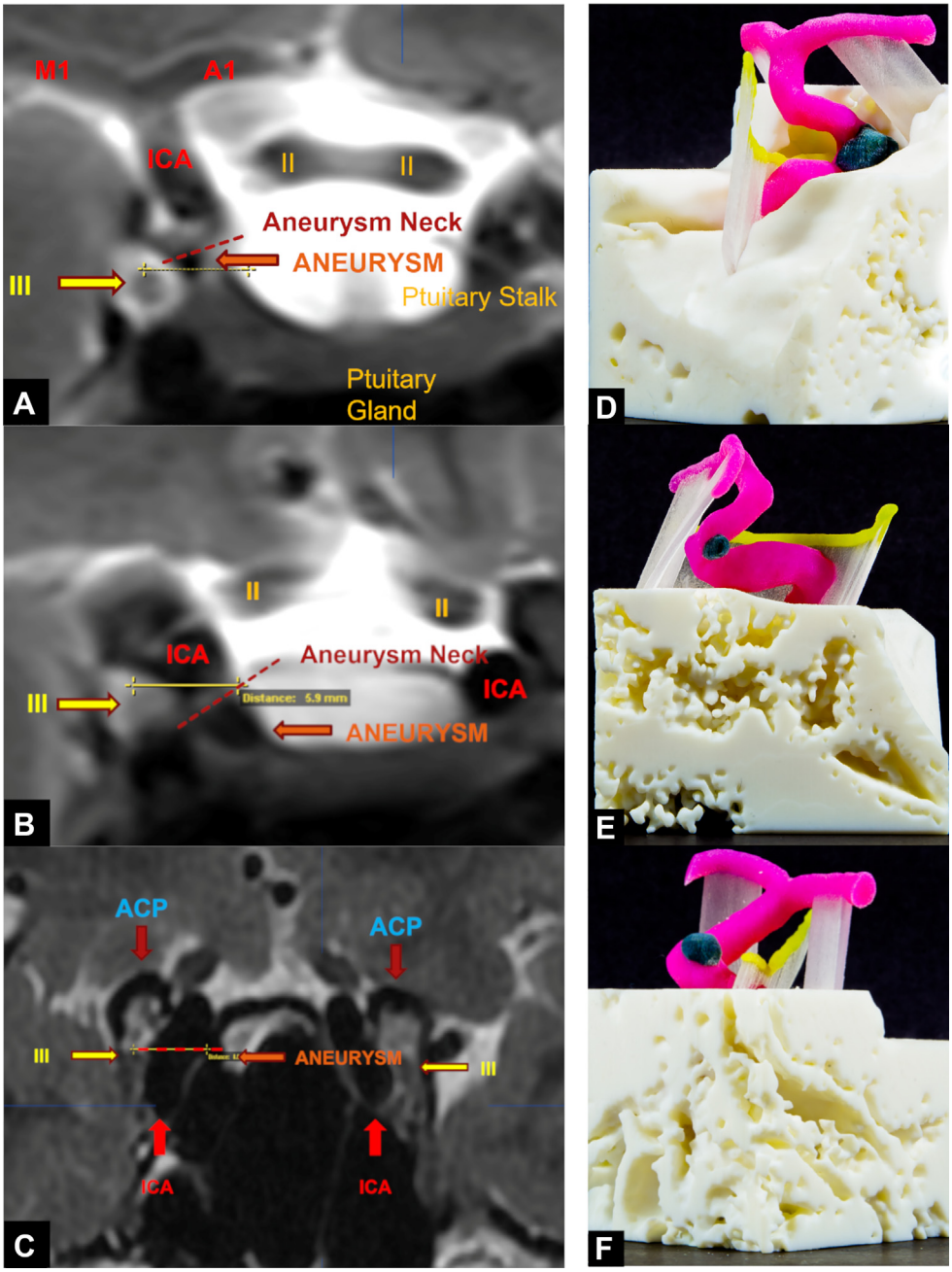

Figure 7. Location of paraclinoid aneurysms in magnetic resonance imaging (MRI) and three-dimensional biomodel. (**A**) Identification of CNIII (oculomotor nerve [third cranial nerve]) (*yellow arrow*) at its intersection with the paraclinoid internal carotid artery (ICA) (*red arrow*) in the cavernous sinus. The *dashed line* connecting the superior limit of the CNIII, laterally, to the ICA, medially, is used for assessment and classification of the intracranial aneurysm (IA) under investigation, classified as superior or extracavernous in this image; the entire neck of the aneurysm is above the superior limit of the CNIII. It is possible to identify the optic nerves (second cranial nerves) (II), pituitary stalk and pituitary gland, M1 and A1. (**B**) Identification of CNIII (*yellow arrow*) at its intersection with paraclinoid ICA (*written in red*) in the cavernous sinus. The optic nerves (II) are identified in *dark yellow*. The *dashed line* connecting the superior limit of the CNIII, laterally, to the ICA, medially, is used for assessment and classification of the IA under investigation, classified as inferior or intracavernous in this image; the entire neck of the aneurysm is inferior the superior limit of the CNIII. (**C**) Identification of CNIII (*yellow arrow*) at its intersection with paraclinoid ICA (*red arrow*) into the cavernous sinus. The anterior clinoid process (ACP) (*blue arrow*) can be seen just above the CNIII. The *dashed line* connecting the superior limit of the CNIII, laterally, to the ICA, medially,

For example, a relationship between the OA or the ACP and paraclinoid aneurysm by digital subtraction angiography was previously proposed.[12] The tuberculum sellae was also hypothetically related to DDR in an anatomic study.[7]

However, these anatomic repairs are not reliable for this purpose. The OA can emerge from the ICA in several locations,[11,21,30,31] and anatomic bone repairs such as ACP, tuberculum sellae, or optic struct are not ideal given the potential anatomic variability in the conformation of the dural rings concerning the ICA. Both rings cross the ICA diagonally with an individual angulation, which prevents the topographic diagnostic accuracy correlated to fixed and indirect anatomic repairs.

Recent studies used 3T MRI to identify the DDR, correlating it to the aneurysmal neck,[17,32-34] although when we hypothetically elect the DDR, we neglect transitional, giant, or paraclinoid aneurysm located in the CC, all of which have SAH risk but are wrongly classified as extradural IA.

A robust study[32] with cadaveric dissections and 3D radiologic imaging evaluation with confirmation intraoperatively in 34 patients proposed a diagnostic method based on bone anatomy supposed to locate the DDR and compare it with the position of paraclinoid aneurysms. Nevertheless, based on this method, aneurysms in the topography of the CC, in the ICA clinoid segment, and/or transitional aneurysms would be mistakenly classified as extradural, without the risk associated with SAH.

The COM cannot be explicitly identified by any diagnostic imaging method, because it is a connective tissue membrane that links the superior limit of CNIII to the ICA. In the anatomic stage, we could identify the superior edge of CNIII at its intersection crossing the entire diameter of the ICA, and we observed the extreme proximity between DDR and COM, or PDR, in the inferior or posterior ICA wall. In addition, we also confirmed the existence of the CC in most anatomic specimens and that the superior limit of CS is formed by the COM, as confirmed in other microanatomic studies.[21,22,35] The proximity between the DDR and COM highlights the importance of choosing the ICA × CNIII as the line for the exact location of paraclinoid IAs, which allows us to delimit the cavernous segment (C4) from the clinoid segment (C5) of the ICA and consequently distinguish intracavernous, transitional, or extracavernous paraclinoid aneurysm. The identification of the ICA × CNIII intersection proved to be reproducible and simple for the identification of COM and the superior delimitation of CS, proving that this is an accurate diagnostic technique, even for small aneurysms or those located in the inferior or posterior ICA wall.

Recent advances in 3D printing technologies have facilitated the creation of biomodels, which play an essential role in neurosurgical preoperative diagnosis and planning. The evaluation of an anatomic structure model in real dimensions allows a clinical view not so easily achieved with conventional imaging methods.[36-38]

In our study, 3D biomodels were used to prove a radiologic diagnostic hypothesis. The practicality of performing 3T MRI/MRA associated with the facility for radiologic identification of the proposed anatomic repairs and the high reliability of 3D biomodel impression allows us to propose a classification of the paraclinoid aneurysm based on the CNIII × ICA, which is not only clinically relevant but is also simple, accurate, and easy to memorize.

The fusion of images acquired from CT of the skull and 3T MRI and 3T MRA in T1, TOF, T2, and FIESTA sequences for clear visualization of each structure in several different planes is essential. Even in the face of a sample with IA of small size, varying between 1.5 mm and 7 mm, only 1 aneurysm was judged to be transitional, classified after evaluation of the 3D biomodel, a fact that corroborates the accuracy of the radiologic method that we propose.

In addition, our study statistically shows through the surrogate mathematical model that the correlations between the evaluators were not casual, which obtained excellent compatibility (95.32%/$P < 0.05$/odds ratio/χ^2/Goodman-Kruskal/κ index) between the radiologic evaluations and the 3D biomodel, and subsequent confirmation through microsurgical direct visualization.

The 2 aneurysms (4.76%) that were considered incompatible indicate that in the absence of direct identification of the PDR, the identification of the superior limit of the CNIII immediately lateral to the ICA, in its entire diameter, and the distance between the CNIII and the ICA can be considered a landmark for delimitation of the roof of the CS, distinguishing intracavernous and extracavernous ICA, because the measurements were close both in anatomic specimens (1.19 mm) and in the patients studied radiologically (1.09 mm).

A literature review of the main articles concludes that we have the largest sample of 42 paraclinoid aneurysms studied. Our study is the only one built in 4 different stages, with the most complete radiologic protocol, with independent and blind evaluations by 2 neuroradiologists, which were confirmed with a 3D-printed biomodel of each IA and with the evaluation of neurosurgical videos based on a thorough statistical analysis, as shown in a comparative table in **Appendix D**.

Among the limitations of this study, we highlight the retrospective data collection and the small sample of aneurysms. Also, most of our IAs were small (3.695 mm on average); studies with a larger sample with bigger or even giant IA and more neuroradiologist evaluators, as well as prospective or real-world studies, can be performed to complement and/or strengthen our findings. In

is used for assessment and classification of the IA under investigation, classified transitional in this image; part of the aneurysmal neck is above and part is inferior to the superior limit of the CNIII. (**D**) Evidence of IA classified as extracavernous or superior to the superior limit of CNIII (*yellow*) at its intersection with the ICA (*pink*). (**E**) Evidence of IA (*black*) classified as intracavernous or inferior the superior limit of CNIII (*yellow*) at its intersection with the ICA (*pink*). (**F**) Evidence of IA classified as transitional, with part of the aneurysmal neck superior and part inferior to the superior limit of CNIII (*yellow*) at its intersection with the ICA (*pink*). In transparent acrylic, the supports for supporting the anatomic structures in their exact anatomic positions were printed after three-dimensional printing.

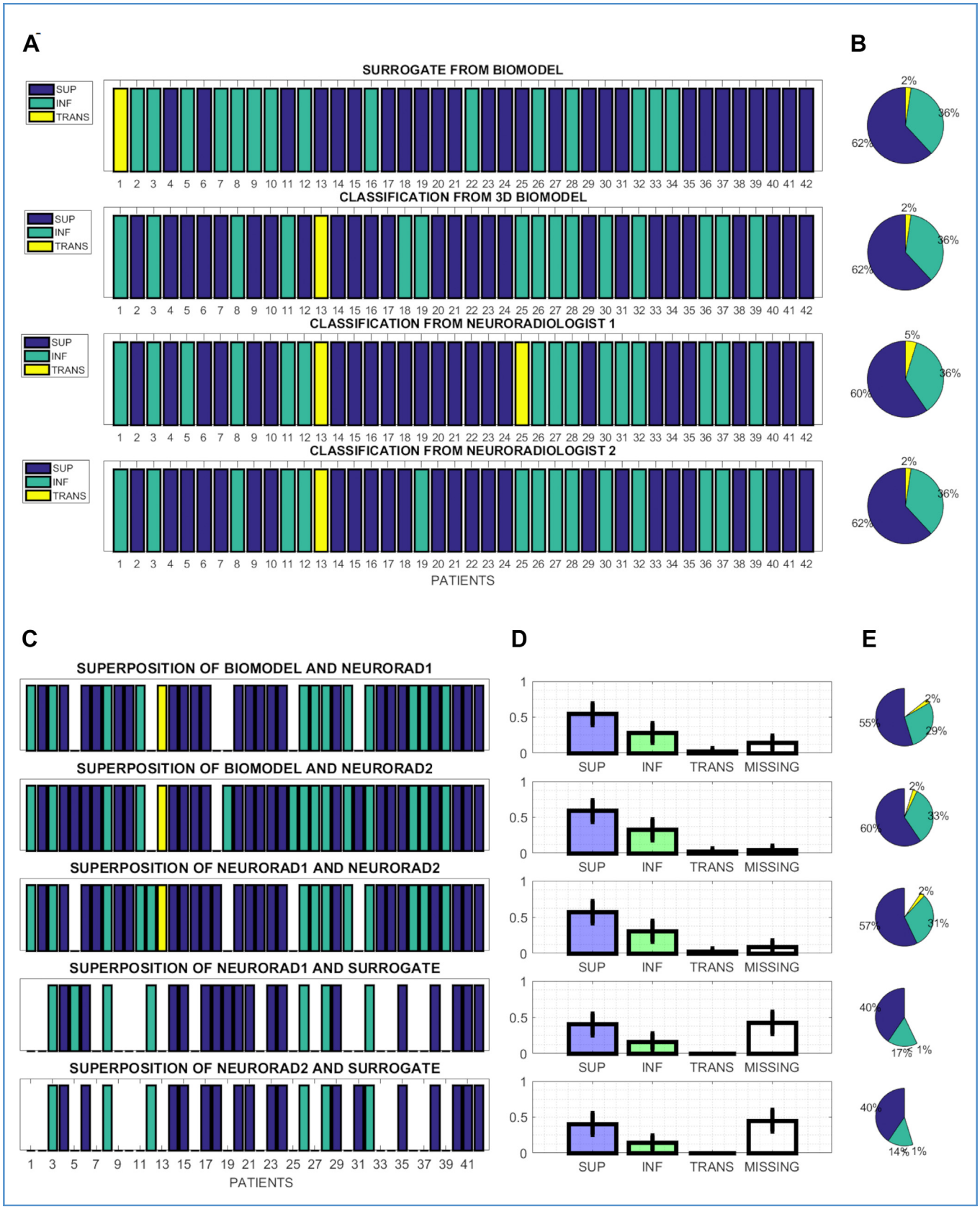
A
SURROGATE FROM BIOMODEL
CLASSIFICATION FROM 3D BIOMODEL
CLASSIFICATION FROM NEURORADIOLOGIST 1
CLASSIFICATION FROM NEURORADIOLOGIST 2
SUP
INF
TRANS
1 2 3 4 5 6 7 8 9 10 11 12 13 14 15 16 17 18 19 20 21 22 23 24 25 26 27 28 29 30 31 32 33 34 35 36 37 38 39 40 41 42
PATIENTS
B
2%
36%
62%
2%
36%
62%
5%
36%
60%
2%
36%
62%
C
SUPERPOSITION OF BIOMODEL AND NEURORAD1
SUPERPOSITION OF BIOMODEL AND NEURORAD2
SUPERPOSITION OF NEURORAD1 AND NEURORAD2
SUPERPOSITION OF NEURORAD1 AND SURROGATE
SUPERPOSITION OF NEURORAD2 AND SURROGATE
1 3 5 7 9 11 13 15 17 19 21 23 25 27 29 31 33 35 37 39 41
PATIENTS
D
1
0.5
0
SUP INF TRANS MISSING
E
55%
2%
29%
60%
2%
33%
57%
2%
31%
40%
17%
1%
40%
14%
1%

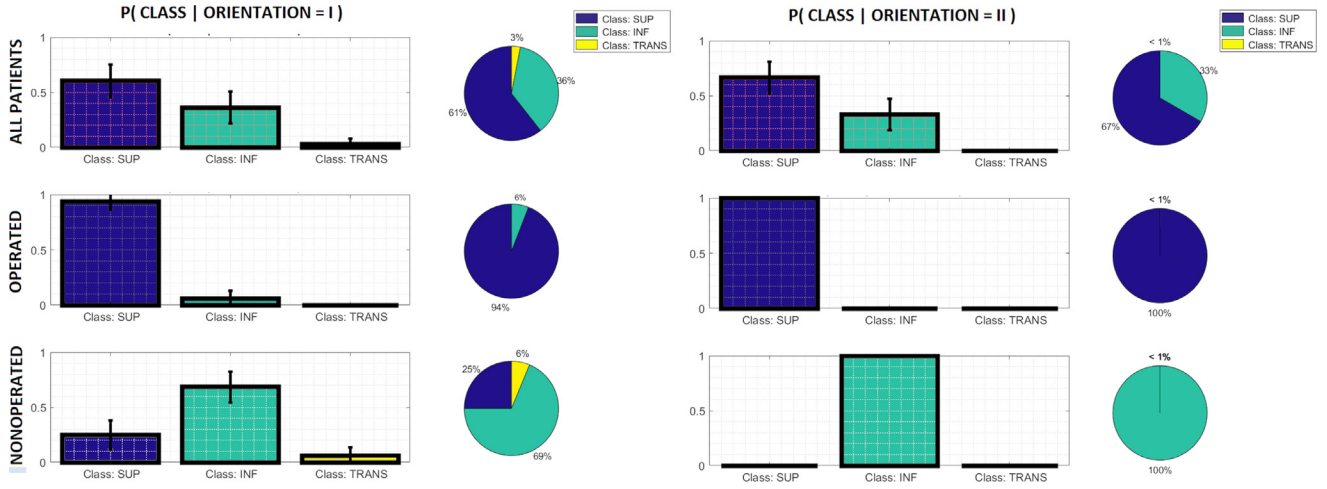

Figure 9. Conditional probabilities (*P*) for each of the 3 classifications given 2 orientations of the aneurysms. Conditional probabilities for an aneurysm to be classified into 1 of the 3 classifications (superior [SUP], inferior [INF], or transitional [TRANS]), considering its orientation in (**A**) type I (located on the medial and inferior or posterior wall of the ICA) or (**B**) type II (located on the lateral and superior or anterior wall of the internal carotid artery), for all patients (*first line*), only operated patients (*second line*), and only nonoperated patients (*third line*). Pie charts show the exact values of the probabilities associated with each class, for each figure opposite.

addition, the evaluation method proposed by 3D biomodels has a relatively high cost and its use is not plausible in some cases, such as in ruptured aneurysms, because they require some time to be printed. However, our MRI protocol is simple, objective, and sequences fusion can be performed quickly, eliminating the need to print the 3D biomodel in cases of lack of time and financial resources.

CONCLUSIONS

We show that the superior limit of the CS is determined by the COM and that there is an intimate relationship of this membrane to the intersection between the ICA and the superior edge of CNIII, which crosses it transversely in its entire diameter. Based on this anatomic landmark, we proposed a new MRI protocol through the radiologic identification of this intersection. Once this intersection is radiologically detected, it is possible to identify the exact distinction between the cavernous and the clinoid ICA segments in its entire diameter, making it easy to distinguish between extracavernous and intracavernous paraclinoid aneurysm.

CRediT AUTHORSHIP CONTRIBUTION STATEMENT

Hugo Leonardo Doria-Netto: Conceptualization, Methodology, Formal analysis, Investigation, Resources, Writing — original draft, Writing — review & editing, Supervision. **Christiane Monteiro de Siqueira Campos:** Conceptualization, Methodology, Investigation, Resources, Writing — original draft, Writing — review & editing. **Victor Hugo Rocha Marussi:** Conceptualization, Methodology, Investigation, Resources, Writing — original draft, Writing — review & editing. **José Maria Campos-Filho:** Conceptualization, Methodology, Investigation, Resources. **Jean Faber:** Conceptualization, Methodology, Formal analysis, Resources, Writing — original draft, Writing — review & editing. **Michael T. Lawton:** Conceptualization, Methodology, Writing — review & editing. **Feres E.A. Chaddad-Neto:** Conceptualization, Methodology, Resources, Writing — review & editing, Supervision.

ACKNOWLEDGMENTS

We are grateful for the support of the Postgraduation Program in Neurology and Neurosciences of UNIFESP, and the Hospital São Paulo and Hospital Beneficência Portuguesa of São Paulo, where this study was conducted.

Figure 8. Classification and classificatory agreement between pairs of evaluators. Color graphic representation of 42 aneurysms classified by neuroradiologists 1 and 2 (NEURORAD1 and NEURORAD2), by the author evaluating the three-dimensional (3D) biomodel and the surrogate mathematical model. (**A**) Classification pattern of each aneurysm by the surrogate model, 3D biomodel, neuroradiologist 1 and neuroradiologist 2, in the 3 classifications of interest: superior (SUP), inferior (INF), and transitional (TRANS). (**B**) Proportion of each of the 3 classifications obtained by the surrogate model, evaluation of the 3D-printed biomodel, neuroradiologist 1 and neuroradiologist 2. (**C**) Overlapping between pairs of classification sequences for evaluation of coincident classifications for each aneurysm. Empty spaces (missing) represent discordant classifications. (**D**) Proportion of patterns remaining in paired comparisons in each of the 3 classifications, and the proportion of disagreements (missing). (**E**) Percentages of comparative agreements between pairs of classifications.

REFERENCES

1. De Jesús O, Sekhar LN, Riedel CJ. Clinoid and paraclinoid aneurysms: surgical anatomy, operative techniques, and outcome. *Surg Neurol*. 1999;51:477-487 [discussion 487-488].
2. Etminan N, Beseoglu K, Barrow DL, et al. Multidisciplinary consensus on assessment of unruptured intracranial aneurysms: proposal of an international research group. *Stroke*. 2014;45:1523-1530.
3. Gonzalez LF, Walker MT, Zabramski JM, Partovi S, Wallace RC, Spetzler RF. Distinction between paraclinoid and cavernous sinus aneurysms with computed tomographic angiography. *Neurosurgery*. 2003;52:1131-1139.
4. Huston J 3rd, Nichols DA, Luetmer PH, et al. Blinded prospective evaluation of sensitivity of MR angiography to known intracranial aneurysms: importance of aneurysm size. *AJNR Am J Neuroradiol*. 1994;15:1607-1614.
5. Kim JM, Romano A, Sanan A, van Loveren HR, Keller JT. Microsurgical anatomic features and nomenclature of the paraclinoid region. *Neurosurgery*. 2000;46:670-680 [discussion 680-682].
6. Nagasawa S, Deguchi J, Arai M, Tanaka H, Kawanishi M, Ohta T. Topographic anatomy of paraclinoid carotid artery aneurysms: usefulness of MR angiographic source images. *Neuroradiology*. 1997;39:341-343.
7. Oikawa S, Kyoshima K, Kobayashi S. Surgical anatomy of the juxta-dural ring area. *J Neurosurg*. 1998;89:250-254.
8. Figueiredo EG, Tavares WM, Rhoton AL Jr, De Oliveira E. Surgical nuances of giant paraclinoid aneurysms. *Neurosurg Rev*. 2010;33:27-36.
9. Gibo H, Lenkey C, Rhoton AL Jr. Microsurgical anatomy of the supraclinoid portion of the internal carotid artery. *J Neurosurg*. 1981;55:560-574.
10. Kyoshima K, Koike G, Hokama M, et al. A classification of juxta-dural ring aneurysms with reference to surgical anatomy. *J Clin Neurosci*. 1996;3:61-64.
11. Taptas JN. Intradural and extradural ICA. *J Neurosurg*. 1979;51:877-878.
12. Punt J. Some observations on aneurysms of the proximal internal carotid artery. *J Neurosurg*. 1979;51:151-154.
13. Hashimoto K, Nozaki K, Hashimoto N. Optic strut as a radiographic landmark in evaluating neck location of a paraclinoid aneurysm. *Neurosurgery*. 2006;59:880-895 [discussion 896-897].
14. Kim MY, Chung SY, Kim SM, Park MS, Jung SS. Determination of aneurysmal location with 3 dimension-computed tomographic angiography in the microsurgery of paraclinoid aneurysms. *J Korean Neurosurg Soc*. 2007;42:35-41.
15. Lee N, Jung JY, Huh SK, Kim DJ, Kim DI, Kim J. Distinction between intradural and extradural aneurysms involving the paraclinoid internal carotid artery with T2-weighted three-dimensional fast spin-echo magnetic resonance imaging. *J Korean Neurosurg Soc*. 2010;47:437-441.
16. Murayama Y, Sakurama K, Satoh K, Nagahiro S. Identification of the carotid artery dural ring by using three-dimensional computerized tomography angiography. Technical note. *J Neurosurg*. 2001;95:533-536.
17. Thines L, Lee SK, Dehdashti AR, et al. Direct imaging of the distal dural ring and paraclinoid internal carotid artery aneurysms with high-resolution T2 turbo-spin echo technique at 3-T magnetic resonance imaging. *Neurosurgery*. 2009;64:1059-1064 [discussion 1064].
18. Matsumoto M, Mizutani T, Sugiyama T, Sumi K, Nakajo T, Arai S. Distance between the falciform ligament and distal dural ring as a surgical landmark for the treatment of paraclinoid aneurysms. *World Neurosurgery*. 2019;124:e498-e502.
19. Seoane E, Rhoton AL Jr, de Oliveira E. Microsurgical anatomy of the dural collar (carotid collar) and rings around the clinoid segment of the internal carotid artery. *Neurosurgery*. 1998;42:869-884 [discussion 884-886].
20. Joo W, Funaki T, Yoshioka F, Rhoton AL Jr. Microsurgical anatomy of the carotid cave. *Neurosurgery*. 2012;70(2 suppl operative):300-311 [discussion 311-312].
21. Rhoton AL Jr. The cavernous sinus, the cavernous venous plexus, and the carotid collar. *Neurosurgery*. 2002;51(4 suppl):S375-S410.
22. Kobayashi S, Kyoshima K, Gibo H, Hegde SA, Takemae T, Sugita K. Carotid cave aneurysms of the internal carotid artery. *J Neurosurg*. 1989;70:216-221.
23. Chaddad-Neto F, Campos Filho JM, Dória-Netto HL, Faria MH, Ribas GC, Oliveira E. The pterional craniotomy: tips and tricks. *Arq Neuropsiquiatr*. 2012;70:727-732.
24. Alejandro SA, Carrasco-Hernández JP, da Costa MDS, et al. Anterior clinoidectomy: intradural step-by-step en bloc removal technique. *World Neurosurg*. 2020;146:217-231.
25. Chaddad-Neto F, Doria-Netto HL, Campos-Filho JM, Ribas ES, Ribas GC, Oliveira E. Head positioning for anterior circulation aneurysms microsurgery. *Arq Neuropsiquiatr*. 2014;72:832-840.
26. Ota N, Petrakakis I, Noda K, et al. Predictor of visual impairment following paraclinoid aneurysm surgery: special consideration of surgical microanatomy related to paraclinoid structures. *Oper Neurosurg (Hagerstown)*. 2020;20:45-54.
27. Matsukawa H, Tanikawa R, Kamiyama H, et al. Risk factors for visual impairments in patients with unruptured intradural paraclinoid aneurysms treated by neck clipping without bypass surgery. *World Neurosurg*. 2016;91:183-189.
28. Kupersmith MJ, Stiebel-Kalish H, Huna-Baron R, et al. Cavernous carotid aneurysms rarely cause subarachnoid hemorrhage or major neurologic morbidity. *J Stroke Cerebrovasc Dis*. 2002;11:9-14.
29. Watanabe Y, Nakazawa T, Yamada N, et al. Identification of the distal dural ring with use of fusion images with 3D-MR cisternography and MR angiography: application to paraclinoid aneurysms. *AJNR Am J Neuroradiol*. 2009;30:845-850.
30. Rhoton AL Jr. The supratentorial arteries. *Neurosurgery*. 2002;51(4 suppl):S53-S120.
31. Rhoton AL Jr. Aneurysms. *Neurosurgery*. 2002;51(4 suppl):S121-S158.
32. Scerbak J, Lapteva O, Sahin OS, et al. Identification of the distal dural ring and definition of paraclinoid aneurysms according to bony landmarks on 3-dimensional computed tomography angiography: a cadaveric and radiological study. *Oper Neurosurg (Hagerstown)*. 2020;19:319-329.
33. Watanabe Y, Makidono A, Nakamura M, Saida Y. 3D MR cisternography to identify distal dural rings: comparison of 3D-CISS and 3D-SPACE sequences. *Magn Reson Med Sci*. 2011;10:29-32.
34. Fernandes ST, Doria-Netto HL, Alves RV, et al. The diagnostic accuracy of MRI in determining the relations between paraclinoid aneurysms and the cavernous sinus. *Neuroradiology*. 2022;64:1175-1185.
35. Yasargil MG, Kasdaglis K, Jain KK, Weber HP. Anatomical observations of the subarachnoid cisterns of the brain during surgery. *J Neurosurg*. 1976;44:298-302.
36. Mardis NJ. Emerging technology and applications of 3D printing in the medical field. *Mo Med*. 2018;115:368-373.
37. Sullivan S, Aguilar-Salinas P, Santos R, Beier AD, Hanel RA. Three-dimensional printing and neuroendovascular simulation for the treatment of a pediatric intracranial aneurysm: case report. *J Neurosurg Pediatr*. 2018;22:672-677.
38. Erbano BO, Opolski AC, Olandoski M, et al. Rapid prototyping of three-dimensional biomodels as an adjuvant in the surgical planning for intracranial aneurysms. *Acta Cir Bras*. 2013;28:756-761.

Conflict of interest statement: The authors declare that the article content was composed in the absence of any commercial or financial relationships that could be construed as a potential conflict of interest.

Received 8 March 2022; accepted 8 August 2022

Citation: World Neurosurg. (2022) 167:e475-e506. https://doi.org/10.1016/j.wneu.2022.08.030

Journal homepage: ***www.journals.elsevier.com/world-neurosurgery***

Available online: ***www.sciencedirect.com***

1878-8750/$ - see front matter

APPENDIX A

STAGES OF THE MICROSURGICAL PROCEDURE

Figure A.1. Neurosurgical images of a patient treated surgically by our team. (**A**) Pterional craniotomy was performed for approaching a right side paraclinoid aneurysm, with evidence in the sylvian fissure located purposely in the center of the craniotomy to favor the transylvian approach. Superiorly to the fissure we have the inferior frontal gyrus and small part of the middle frontal gyrus. Inferior to the fissure we have the superior

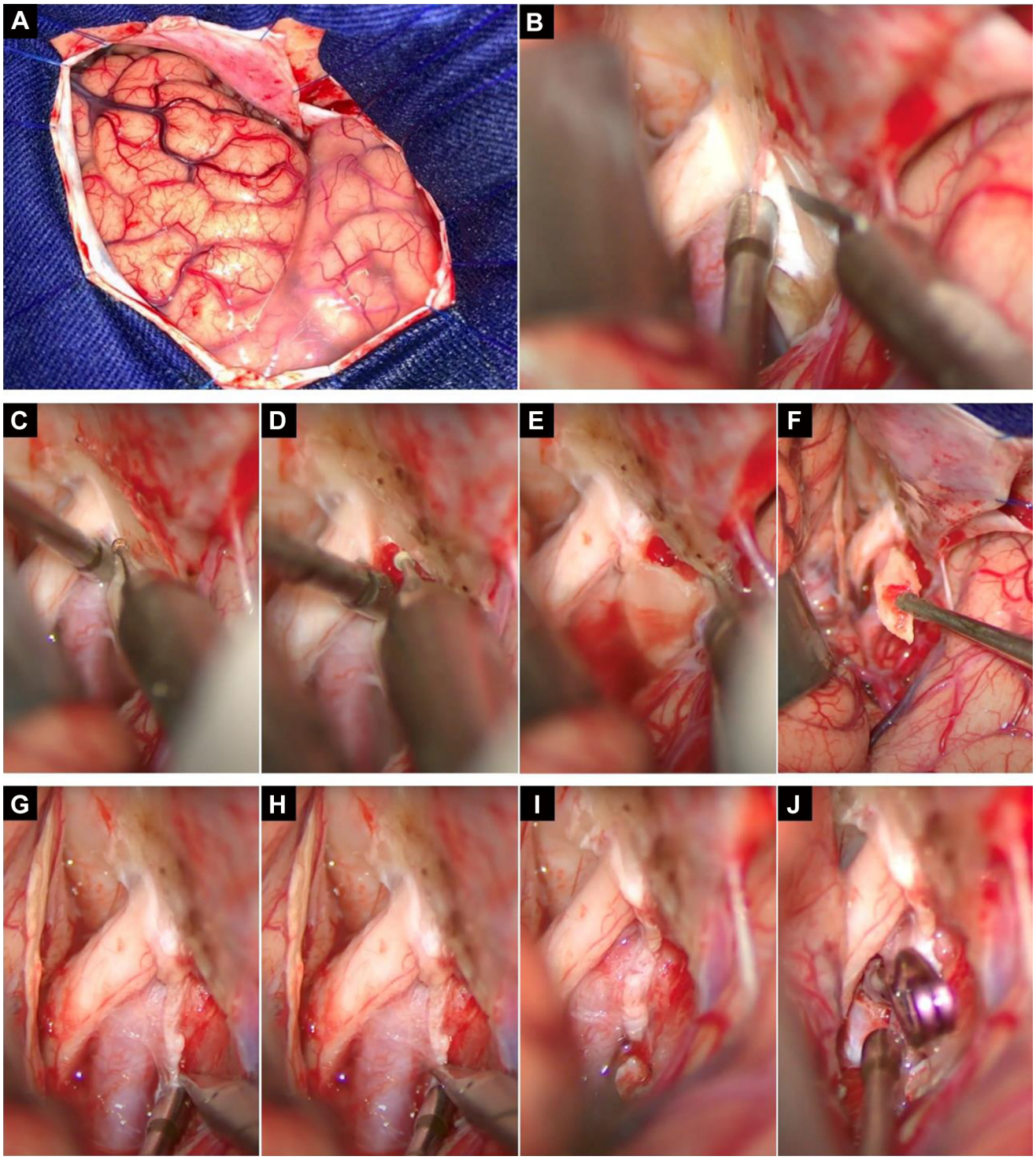

temporal gyrus and a small part of the middle temporal gyrus. It is important to note the total rectification of the superior orbital rim obtained after drilling it, which gives enlargement of the lateral subfrontal approach. (**B**) Arciform dural incision over the anterior clinoid process (ACP), performed with an 11-blade scalpel, from medial to the optic nerve (OpN) to the lateral part of the ACP with caution so that there is no inadvertent injury to the OpN and CNIII. (**C**) and (**D**) After drilling initially in the medial part to OpN and disconnecting the ACP from the sphenoid planum and roof of the optic canal, medially, we started drilling over the ACP to disconnect it from the smaller sphenoid wing, laterally. Note the positioning of the head, in which there is no extension of the head, favoring perpendicular access to the upper part of ACP, from top to bottom, favoring its drilling, to perform the anterior clinoidectomy. (**E**) and (**F**) End of disconnection of the ACP from the smaller wing of the sphenoid bone, laterally, disconnecting the ACP from its medial and inferior edge, the optic struct (OpS), we will have all 3 points of the ACP disconnected, being the sphenoid planum, medially and superiorly, the OpS, medially and inferiorly, and the smaller wing of the sphenoid bone, laterally, culminating in the anterior clinoidectomy, well shown in (**F**). (**G**) and (**H**) After the anterior clinoidectomy, we proceeded to the next neurosurgical step, the opening of the OpN sheath and the incision of the falciform ligament, both performed to release and mobilize the OpN superiorly and medially. Then, we performed the opening of the distal dural ring (DDR). This is well visualized in (**G**) and (**H**) with emphasis on cutting the DDR with the microscissors perpendicular to the internal carotid artery (ICA) with the ICA being released for its inferior and lateral mobilization, expanding the optical-carotid space. (**I**) Wide exposure of the ICA in clinoid (C_5) and ophthalmic (C6) segments. carotid-oculomotor membrane (COM) exhibition linking CNIII to ICA showing the entire intersection between ICA and CNIII. It is possible to verify that the line from the superior limit of CNIII, laterally, to the ICA, medially, is coincident to the COM and conclude that this line is the intersection between the ICA and the CNIII. We note the presence of the carotid collar, between the DDR and the COM without evidence of hemorrhage from the cavernous sinus, which has not been violated and is found inferiorly to the superior limit of the intersection between the CNIII and the ICA. (**J**) Clipping, without complications, of intracranial aneurysm in topography of paraclinoid ICA, medial and inferior wall, distally to the DDR, in this case.

APPENDIX B

DISTANCES BETWEEN ANATOMIC STRUCTURES

In the dissections of cadaveric specimens, we showed different distances between the distal dural ring and proximal dural ring measured on the superior and inferior walls of the internal carotid artery (ICA), with a mean of 5.04 mm (range, 4–6 mm) and 1.26 mm (range, 0 .9–2 mm), respectively, proving the extreme proximity between these structures on the inferior or posterior wall of the ICA.

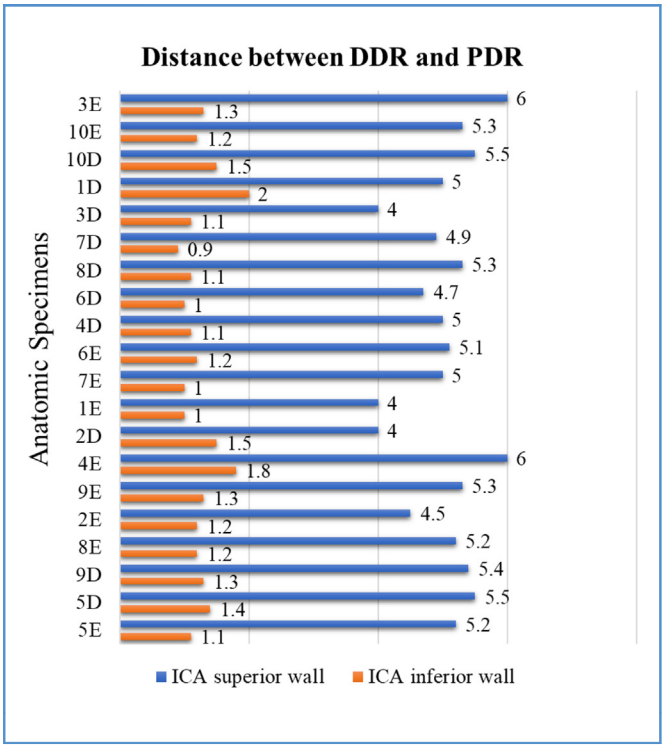

Figure B.1. Distance (mm) between distal dural ring and proximal dural ring measured on the superior (arithmetic mean, 5.04 mm) and inferior (arithmetic mean, 1.26 mm) walls of the internal carotid artery (ICA). There is an anatomic conformation of the diagonal placement of the dural rings on the ICA, because we observed a proportion of 4:1 between measurements of the distances between dural rings and the different internal carotid artery walls.

It was also possible to identify the superior limit of CNIII at its intersection with the entire diameter of the ICA, because we showed the average distance between ICA and CNIII, at their intersection, of 1.19 mm (range, 0.6–1.7 mm) in the 20 brain hemispheres dissected in 10 anatomic specimens and 1.09 mm (range, 0.4–2.6 mm) and in the 67 cavernous sinuses of the 34 patients studied radiologically.

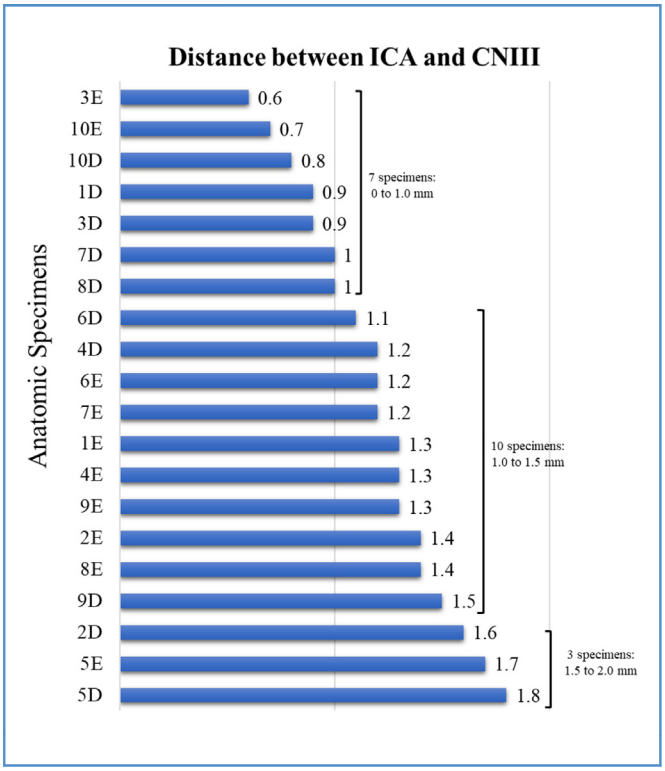

Figure B.2. Distance (mm) between internal carotid artery and CNIII (oculomotor nerve) in the cadaveric specimens studied with stratification by range. Arithmetic mean, 1.19 mm.

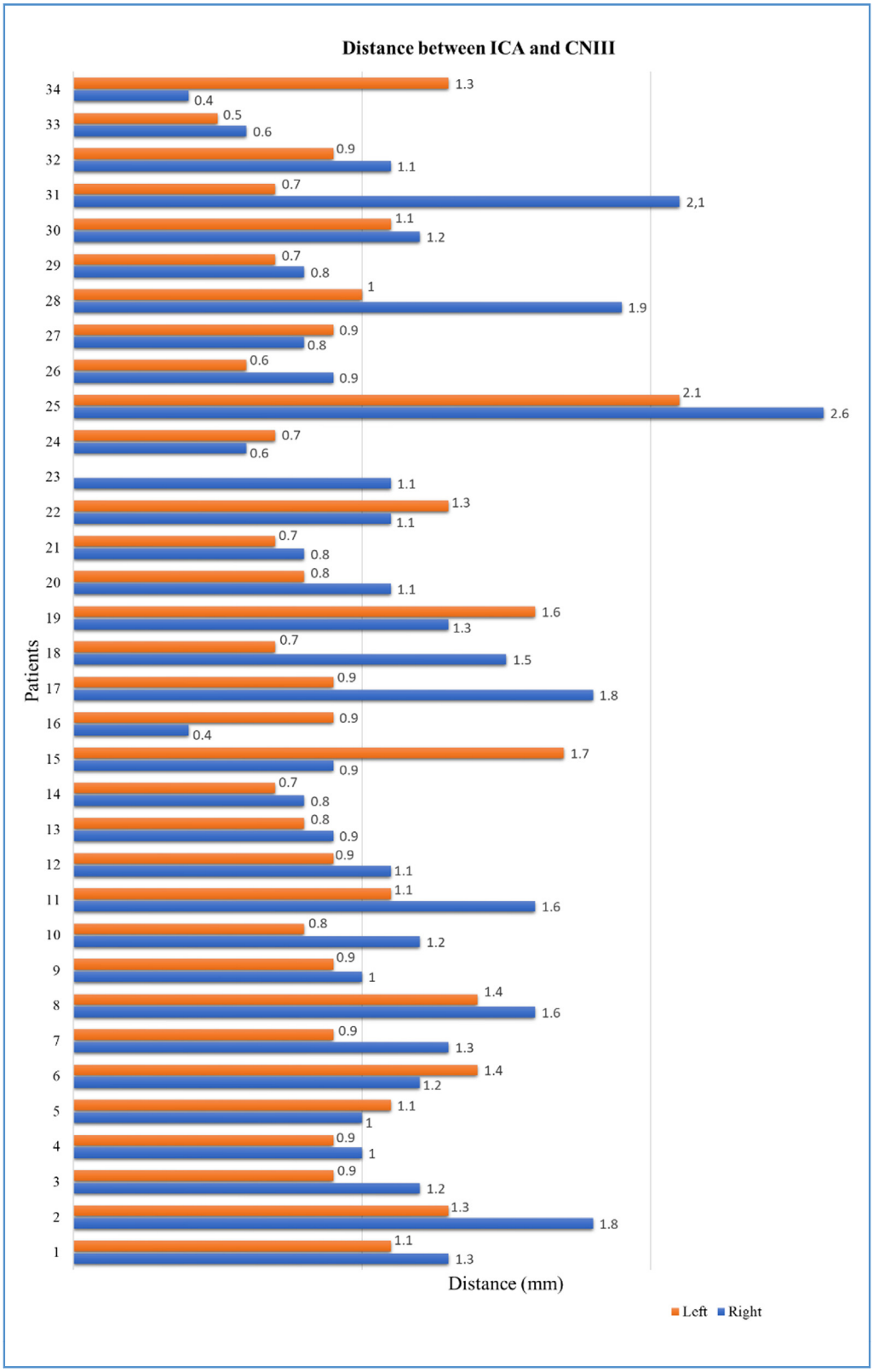
Distance between ICA and CNIII
Patients
Distance (mm)
Left
Right
34 1.3 0.4
33 0.5 0.6
32 0.9 1.1
31 0.7 2,1
30 1.1 1.2
29 0.7 0.8
28 1 1.9
27 0.9 0.8
26 0.6 0.9
25 2.1 2.6
24 0.7 0.6
23 1.1
22 1.3 1.1
21 0.7 0.8
20 0.8 1.1
19 1.6 1.3
18 0.7 1.5
17 0.9 1.8
16 0.9 0.4
15 1.7 0.9
14 0.7 0.8
13 0.8 0.9
12 0.9 1.1
11 1.1 1.6
10 0.8 1.2
9 0.9 1
8 1.4 1.6
7 0.9 1.3
6 1.4 1.2
5 1.1 1
4 0.9 1
3 0.9 1.2
2 1.3 1.8
1 1.1 1.3

Figure B.3. Distance between anatomic structures on radiologic images of patients. Distance (mm) between right (*orange bars*) and left (*blue bars*) internal carotid artery (ICA) and CNIII (oculomotor nerve) measured in the image segmentation process. The arithmetic means of the distances between the right ICA and the CNIII was 1.176 mm (range, 0.4–2.6 mm). The arithmetic means of the distances between the left ICA and the CNIII was 1.009 mm (range, 0.5–2.1 mm). Among the measurements of the distances between the left ICA and the CNIII, we considered a total of 34 patients, with 67 measurements. In 1 patient (patient 23), on the left side, in which there was no intracranial aneurysm paraclinoid, the accurate visualization of the superior limit of the CNIII in its cavernous course at the point of intersection with the ICA was not adequate in radiologic images. Therefore, this side was excluded from the evaluation.

APPENDIX C

STATISTICAL ANALYSIS BETWEEN ANEURYSMS CLASSIFICATION

To exclude randomness in the analysis of agreement between classifications, a surrogate data was generated by randomly shuffling the three-dimensional (3D) biomodels classification. For analysis of agreement between the radiologic and 3D biomodel classifications, Goodman-Kruskal γ test, odds ratio, χ^2, κ index, and discordance ratio tests were performed, with a confidence interval (CI) of 95%, and statistical significance was considered for values with $P \leq 0.05$. The CI was calculated using the binomial distribution CI (P, 95%) = $\pm 1.96\sqrt{(p(1-p)/n)}$. B, 3D biomodel; R1, neuroradiologist 1; R2, neuroradiologist 2; S, surrogate model.

patients as transitional (TRANS) (transitional, OR, 0.4878; 95% CI, 0.2664–0.7542; $P < 0.001$). In the second graph, no difference between the classification proportions in the 3 classes between neuroradiologist 2 (NEURORAD2) and the 3D biomodel (OR, 1.0; 95% confidence interval [CI], 0.5461–1.546; $P < 0.001$) was observed. In the third graph, a difference is observed only in the proportions of the transitional class when comparing the classifications between the 2 neuroradiologists (superior, OR, 0.9050, 95% CI, 0.4942–1.3992, $P < 0.001$; inferior, OR, 1, 0, 95% CI, 0.5461–1.5461, $P < 0.001$; transitional, OR, 2.0500, 95% CI, 1.1196–3.1696, $P < 0.001$). The fourth graph (superior, OR, 1.1050, 95% CI, 0.6035–1.7085, $P = 0.7345$; inferior, OR, 1.0, 95% CI, 0.5461–1.5461, $P = 0.8103$; transitional, OR, 0.4878, 95% CI, 0.2664–0.7542, $P = 0.8210$)

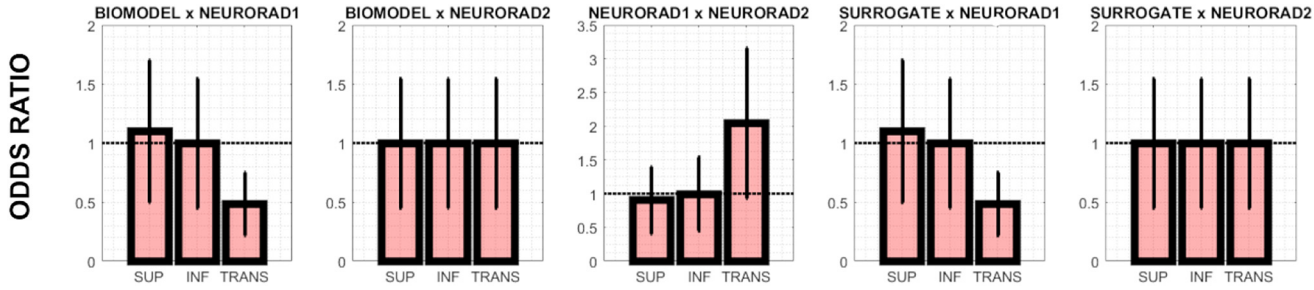

Figure C.1. Odds ratio test. Applying the odds ratio test and the χ^2 test, it is possible to observe in the first graph that the proportion of classifications between the three-dimensional (3D) biomodel and neuroradiologist 1 (NEURORAD1) is similar for superior (SUP) and inferior (INF) ophthalmic artery (superior, odds ratio [OR], 1.1050, 95% confidence interval [CI], 0.6035–1.7085, $P < 0.001$; inferior, OR, 1.0, 95% CI, 0.5461–1.5461, $P < 0.001$), showing the difference in the proportion of classified shows the same pattern as the first graph, and the pattern of the fifth graph (superior, OR, 1.0, 95% CI, 0.5461–1.5461, $P = 0.5539$; inferior, OR, 1.0, 95% CI, 0.5461–1.5461, $P = 0.6657$; transitional, OR, 1.0, 95% CI, 0.5461–1.5461, $P = 0.8744$) also shows similarity with the second graph. Once the surrogate model is generated from the classification pattern of the 3D biomodel by shuffling its sequence, the surrogate model maintains the same proportion of identified classes, however, without statistical significance.

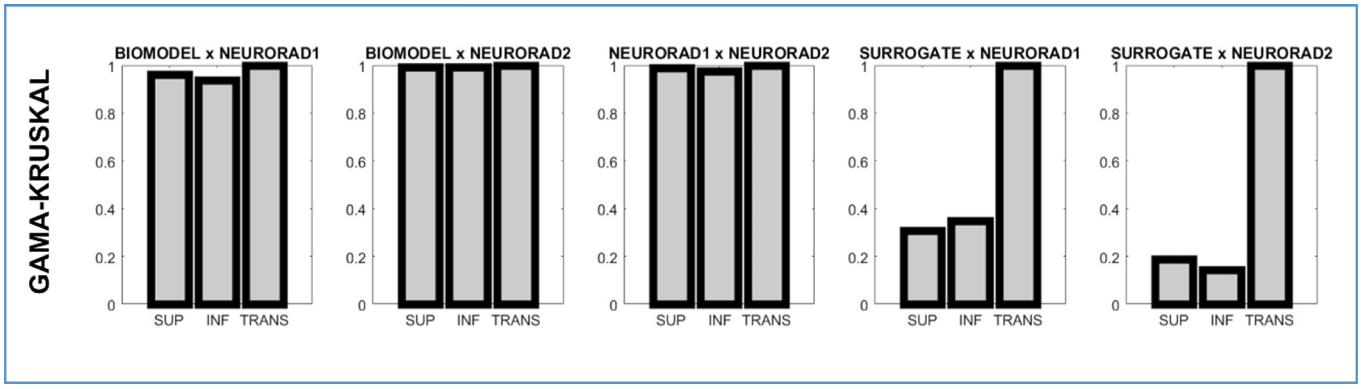

Figure C.2. γ-Kruskal association index test. Using the γ-Kruskal association index and the t test, the same pairs of raters were compared. In the first graph, we observed high agreement comparing the classifications of the three-dimensional (3D) biomodel and neuroradiologist 1 (NEURORAD1) (superior [SUP], G index, 0.9634, $P < 0.001$; inferior [INF], G index, 0.9394, $P < 0.001$; transitional [TRANS], G index, 0.9999, $P < 0.001$). In box 2, comparing the classifications of the 3D biomodel and neuroradiologist 2 (NEURORAD2), shows the greatest agreement, with indices close to 1 for the 3 classes (superior, inferior, and transitional). In box 3, comparing the classifications of neuroradiologists 1 and 2, we found great agreement. In boxes 4 and 5, the classifications performed by the surrogate model compared with neuroradiologists 1 and 2, respectively, show low agreement between the superior and inferior classes. There is, supposedly, high agreement in the evaluation of the transitional class, because the sample number is very low and the proportion between the surrogate and the 3D biomodel is the same.

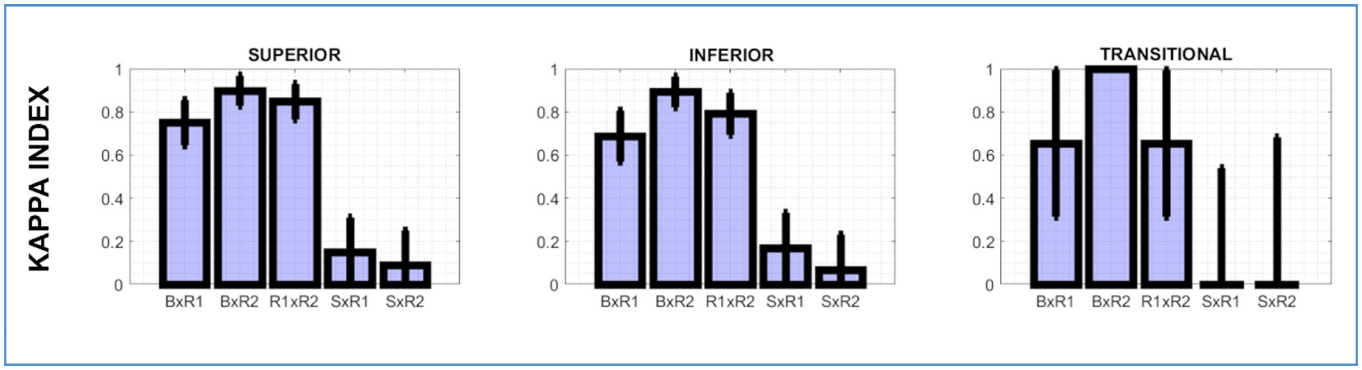

Figure C.3. κ association index test. Using the κ association index, we observed high agreement between the classifications of the biomodel, neuroradiologist 1 and neuroradiologist 2, with variations within the confidence intervals. The classifications with the highest agreement are between the biomodel and the neuroradiologist 2 (superior, κ 0.8990, 95% confidence interval [CI], 0.0697–0.9687; inferior, κ 0.8963, 95% CI, 0.0716–0.9679; transitional, κ 1.0, 95% CI, 0–1.0000), between neuroradiologists 1 and 2 (superior, κ 0.8504, 95% CI, 0.0833–0.9336; inferior, κ 0.7926, CI 95% 0.0986–0.8912; transitional, κ 0.6557, 95% CI, 0.3401–0.9999), and between biomodel and neuroradiologist 1 (superior, κ 0.7506, 95% CI, 0.1047–0.8553; inferior, κ 0.6889, 95% CI, 0.1176–0.8065; transitional, κ 0.6557, 95% CI, 0.3401–0.9999), respectively. Note that there is no agreement between the classifications of the surrogate model and neuroradiologist 1 (superior, κ 0.0523, 95% CI, 0.1609–0.2132; inferior, κ 0.1704, 95% CI, 0.1632–0.3336; transitional, κ 0.0328, 95% CI, 0.5746–0.5418) and between the surrogate model and neuroradiologist 2 (superior, κ 0.0913, 95% CI, 0.1619–0.2532; inferior, κ 0.1704, 95% CI, 0.1632–0.3336; transitional, κ 0.0244, 95% CI, 0.7069–0.6825), for the superior and transitional classes, with evidence of confidence intervals distinct. There is a lack of agreement between the classifications of AI as inferior between the surrogated model and neuroradiologists 1 and 2, despite coincident CIs.

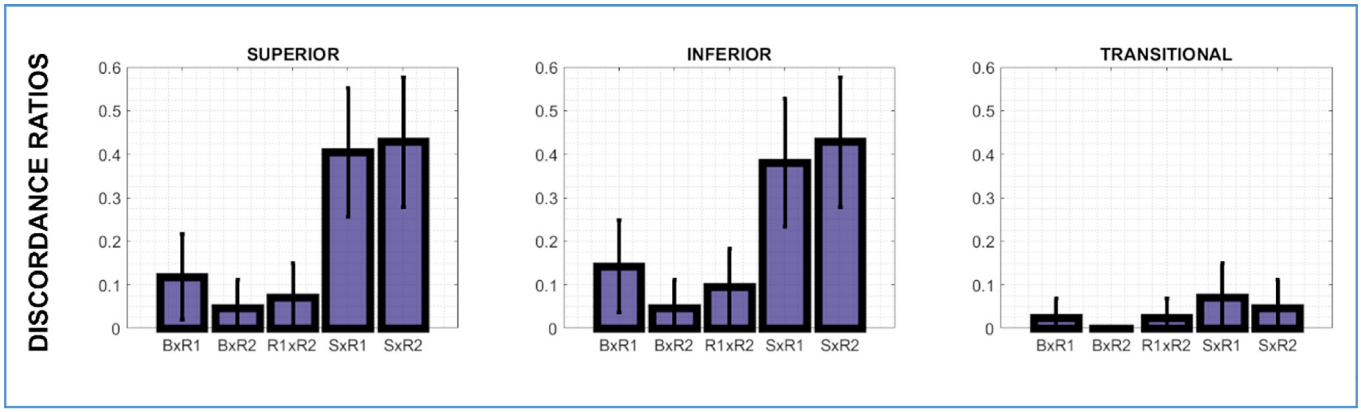

Figure C.4. Discordance ratio (DR) test. The DR shows very low disagreement for the classification of aneurysms when evaluating the comparisons between the three-dimensional (3D) biomodel and neuroradiologist 1 (superior, DR, 0.1190, 95% confidence interval [CI], 0.0211–0.2170; inferior, DR, 0.1429, 95% CI, 0.0370–0.2487; transitional, DR, 0.0238, 95% CI, −0.0223 to 0.0699), between the 3D biomodel and the neuroradiologist 2 (superior, DR, 0.0476, 95% CI, −0.0168 to 0.11120; inferior, DR, 0.0476, 95% CI, −0.0168 to 0.1120; transitional, DR, 0.0), and between neuroradiologists 1 and 2 (superior, DR, 0.0714, 95% CI, −0.0065 to 0.1493; inferior, DR 0.0952, 95% CI, 0.0065–0.1840; transitional, DR 0.0238, 95% CI, −0.0223 to 0.0699). It is possible to observe a higher level of disagreement between the surrogate model and neuroradiologist 1 (superior, DR, 0.5000, 95% CI, 0.3488–0.6512; inferior, DR, 0.4286, 95% CI, 0.2789–0 .5782; transitional, DR, 0.0714, 95% CI, −0.0065 to 0.1493), and between the surrogate model and neuroradiologist 2 (superior, DR, 0.5714, 95% CI, 0.4218–0.7211; inferior, DR, 0.5238, 95% CI, 0.3728–0.6749; transitional, DR, 0.0476, 95% CI, −0.0168 to 0.1120).

To statistically prove the agreement between the classifications, t test and χ^2 test were applied to the Goodman-Kruskal γ index and the odds ratio test, respectively. Appling the odds ratio test, it is possible to observe that the proportions of classifications between the 3D biomodel and each neuroradiologist are similar for superior intracranial aneurysm. Using the γ-Kruskal, κ, and generated from the 3D biomodel classification pattern by shuffling its sequence, it maintains the same proportion of identified classes, however, without statistical significance. On the other hand, there was no statistical agreement or similarity between each radiologist and the surrogate model. Therefore, we can exclude randomness as a possible bias in our study.

Table C.1. *P* Values of Agreement Odds Ratio and γ-Kruskal Tests

		Superior		Inferior		Transitional	
Classification	**Statistical Tests**	**Test Index**	***P* Value**	**Test Index**	***P* Value**	**Test Index**	***P* Value**
B × R1	Odds ratio	1.1050	<0.01	1.0000	<0.01	0.4878	<0.01
	γ-Kruskal	0.9634	<0.01	0.9394	<0.01	0.9999	<0.01
B × R2	Odds ratio	1.0000	<0.01	1.0000	<0.01	1.0000	<0.01
	γ-Kruskal	0.9947	<0.01	0.9945	<0.01	0.9999	<0.01
R1 × R2	Odds ratio	0.9050	<0.01	1.0000	<0.01	2.0500	<0.01
	γ-Kruskal	0.9890	<0.01	0.9757	<0.01	0.9999	<0.01
R1 × S	Odds ratio	1.1050	0.73	1.0000	0.81	0.4878	0.82
	γ-Kruskal	0.1089	0.38	0.0811	0.39	0.9999	<0.01
R2 × S	Odds ratio	1.0000	0.55	1.0000	0.67	1.0000	0.87
	γ-Kruskal	0.1900	0.36	0.1429	0.38	0.9999	<0.01

B, biomodel, R1, radiologist 1; R2, radiologist 2; S, surrogate model.

disagreement ratio, it is possible to observe high agreement between the 3D biomodel and the neuroradiologists classifications. t test and χ^2 were applied to Goodman-Kruskal γ index and odds ratio test, respectively, emphasizing the agreement between the pairs of clinical classifications. Once the surrogate data were

In addition, to analyze the agreement between evaluators for classification of operated and nonoperated aneurysms, the estimate of the odds ratio was performed with a confidence interval of 95%, and statistical significance was considered for values with $P \leq 0.05$.

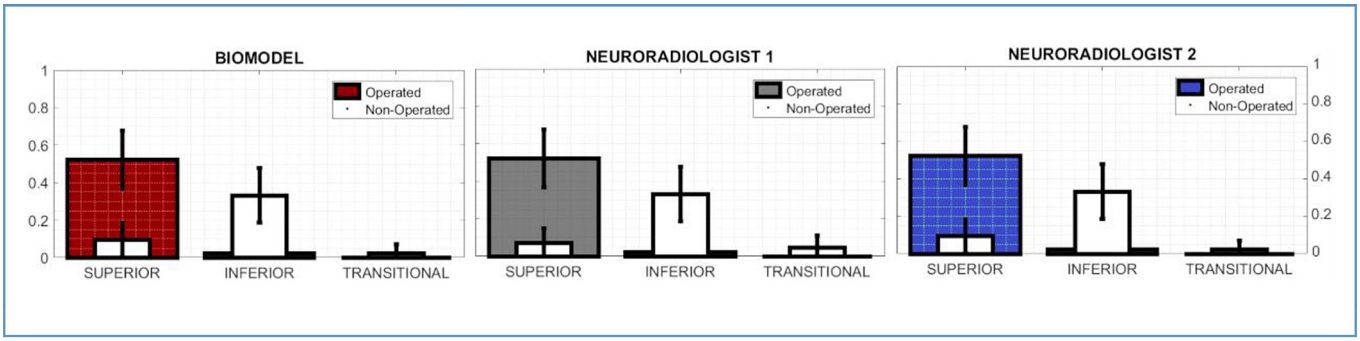

Figure C.5. Proportions of aneurysm classifications for operated and nonoperated patients. Among the operated and nonoperated aneurysms, there was no disagreement between the evaluators for any of the operated aneurysms, and a similar proportion was found in the classification of nonoperated aneurysms. It is possible to observe similar proportions among the 3 evaluators in the classification of operated aneurysms classified as superior and inferior (superior, 0.5238, 95% confidence interval [CI], 0.3697–0.6779; inferior, 0.0238, 95% CI, −0.0232 to 0.0709) and nonoperated aneurysms classified as inferior (0.3333, 95% CI, 0.1879–0.4788). There is a small difference between aneurysms classified as superior and transitional by neuroradiologist 2 (superior, 0.0714, 95% CI, −0.0080 to 0.1509; transitional, 0.0476, 95% CI, −0.0181 to 0.1133) compared with the 3D biomodel and with neuroradiologist 2, who obtained similar proportions for the classification of superior and transitional aneurysms (superior, 0.0952, 95% CI, 0.0046–0.1858; transitional, 0.0238, 95% CI, −0.0232 to 0.0709).

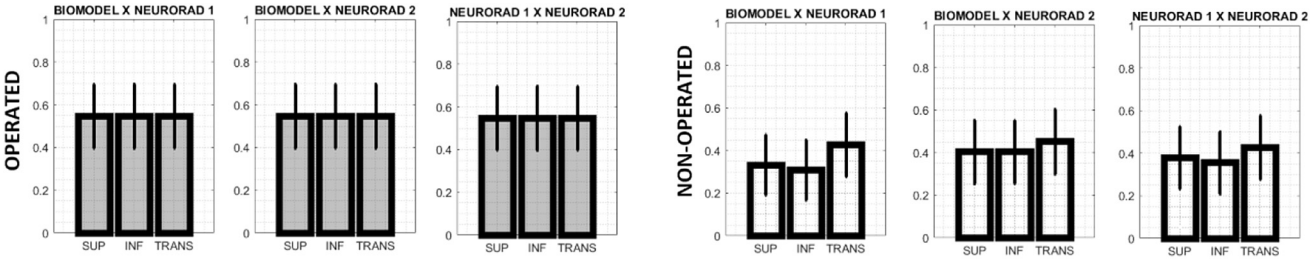

Figure C.6. Agreement test for operated and nonoperated patients. Statistical analysis using the odds ratio scale and χ^2 test showed a statistically significant correlation between the evaluations of neuroradiologists 1 (*NEURORAD1*) and 2 (*NEURORAD2*), and the printed three-dimensional (3D) biomodel, with P value <0.05. Among the operated aneurysms, we observed complete agreement between the evaluations obtained by the 3D biomodel, neuroradiologist 1 and neuroradiologist 2, for the 3 classes of aneurysms (0.5476; 95% confidence interval [CI], 0.3971–0.6981; $P < 0.01$). Among nonoperated aneurysms, there was greater agreement between the 3D biomodel and neuroradiologist 2 (superior [*SUP*], 0.3810, 95% CI, 0.2341–0.5278, $P < 0.05$; inferior [*INF*], 0.3571, 95% CI, 0, 2122–0.5021, $P < 0.05$; transitional [*TRANS*], 0.4286, 95% CI, 0.2789–0.5782, $P < 0.01$) and between neuroradiologist 1 and neuroradiologists 2 (superior, 0.4048, CI 95% 0.2563–0.5532, $P < 0.05$; inferior, 0.4048, 95% CI, 0.2563–0.5532, $P < 0.05$; transitional, 0.4524, 95% CI, 0.3019– 0.6029, $P < 0.01$) compared with the 3D biomodel versus neuroradiologist 1 (superior, 0.3333, 95% CI, 0.1908–0.4759, $P = 0.56$; inferior, 0.3095, 95% CI, 0.1697–0.4493, $P = 0.41$; transitional, 0.4286, 95% CI, 0.2789–0.5782, $P < 0.01$).

All these tests show that there is strong agreement between the neuroradiologists and the 3D biomodel, when evaluated by peers, and that there is no agreement between the surrogate model and the classifications of the neuroradiologists. Furthermore, there was complete agreement between the findings obtained through direct microsurgical visualization and the classification obtained through the printed 3D biomodel and the radiologic classifications obtained through the evaluations of neuroradiologists 1 and 2. These findings indicate that the radiologic classification proposed in this study is not only easy but also accurate, distinguishing intracavernous internal carotid artery and extracavernous ICA.

APPENDIX D

COMPARATIVE TABLE OF METHODS AND LANDMARKS FOR DISTINGUISHING PARACLINOID ANEURYSMS

Reference	Anatomic Landmark	Limitations	Evaluation Method	Anatomic (Number of Specimens)	Radiologic (Number of Aneurysms/ Patients)	Evaluators (Number of Evaluators)	3D (Number of Aneurysms/ Patients)	Surgical (Number of Aneurysms/ Patients)	Statistical Method
Punt, 1979[1]	The angiographic origin of the ophthalmic artery	There is a wide variability of the origin of the ophthalmic artery	Bilateral carotid angiography (n = 36) and vertebral angiography (n = 10)	—	41 IA/36 patients	—	—	—	—
Taptas, 1979[2]	Correlation between ACP and paraclinoid IA	Great morphologic variability of ACP and ICA	—	—	—	—	—	—	—
Oikawa et al., 1998[3]	The superior edge of ACP and the tuberculum sellae	There is great variability of the positioning of the DDR in the ICA and there is a weak relationship with bone structures	Anteroposterior and lateral plain radiography film	20 cerebral hemispheres	—	—	—	—	—
Murayama et al., 2001[4]	The concavity of the paraclinoid segment of the ICA	Atheromatous plaques, calcifications, artifacts or distortions of the ICA wall in the presence of large or giant aneurysms/ICA atherosclerosis/ fibromuscular dysplasia	3D CT angiography	—	5 IA/5 patients	2 examiners	—	1 IA/1 patient	—
Ito et al., 2002[5]	The evaluation of vascular structures close to the bone, such as the branch point of the ophthalmic artery and the limit of the CS	Anatomic distortions/ bone artifacts/giant aneurysms	3D CE CT cisternography	—	1 IA/1 patient	—	—	1 IA/1 patient	—
Gonzalez et al., 2003[6]	The optic strut as an anatomic landmark for accurate discrimination between intradural and extradural (CS) aneurysms	The optic strut does not relate to the entire diameter of the ICA, but only to its anterior and superior wall	CT angiography	10 cerebral hemispheres	6 IA/4 patients	2 neuroradiologists	—	—	—
Beretta et al., 2004[7]	DDR inference through identification of sphenoid plane, tuberculum sellae and optic canal for differentiating	Complex or giant aneurysms can distort the anatomic features by eroding normal osseous structures and	Plain digital radiographs (planum view and lateral view) - biplanar angiographic C-arm	5 cadaveric heads 50 dry skulls	—	—	—	—	—

IA, intracranial aneurysm; ACP, anterior clinoid process; DDR, distal dural ring; 3D- ICA, internal carotid artery; 3D, three-dimensional; CE, contrast-enhanced; MRA, magnetic resonance angiography; CT, computed tomography; CS, cavernous sinus; TOF, time of flight, CISS, constructive interference in steady state; MRI, magnetic resonance imaging; SPACE, turbo spin echo sequence sampling perfection with application-optimized contrasts using different flip angle evolution.

Continues

Continued

Reference	Anatomic Landmark	Limitations	Evaluation Method	Anatomic (Number of Specimens)	Radiologic (Number of Aneurysms/ Patients)	Evaluators (Number of Evaluators)	3D (Number of Aneurysms/ Patients)	Surgical (Number of Aneurysms/ Patients)	Statistical Method
	paraclinoid region aneurysms into extradural (proximal to the DDR) or intradural (distal to the DDR)	violating traditional anatomic boundaries							
Hashimoto et al., 2006[8]	The accuracy of the optic strut as a landmark for image examination during preoperative evaluation of a paraclinoid aneurysm	The optic strut does not relate to the entire diameter of the ICA, but only to its anterior and superior wall	3D CT angiographic	—	18 IA/17 patients	1 neurosurgeon and 1 neuroradiologist	—	18 IA/17 patients	—
Tsuboi et al., 2006[9]	The location of aneurysms using CE MRA, as either intradural or extradural, was examined by, positional interrelation between the aneurysm dome, neck and CS	Might have limitations in displaying the dura mater. The clear delineation of the superior wall should be important in distinguishing intradural location from extradural location of aneurysms	CE 3D MRA 1.5T TOF T1 (CS)	—	24 IA/21 patients	—	—	7 IA/7 patients	—
Hirai et al., 2008[10]	Using CE 3D-CISS MRI for the differentiation between paraclinoid and CS aneurysms	Misinterpretation of the location of carotid cave, giant or multiple aneurysms. Difficulty to distinguish superior boundary of CS when there was high signal intensity of blood into giant paraclinoid aneurysm	CE 3D CISS MRI identification of superior boundary of CS	—	11 IA/10 patients	2 neuroradiologists	—	11 IA/10 patients	—
Thines et al., 2009[11]	The feasibility of the direct visualization of the DDR and adjacent anatomic structures in patients with paraclinoid internal carotid artery aneurysms at 3T MRI	Limitation of the imaging technique is the spatial and contrast resolution of MRI. Another potential difficulty is the precise localization of small carotid cave aneurysms. Difficulty to identify the DDR in all patients	3T MRI	—	7 IA/6 patients	1 neuroradiologist and 1 neurosurgeon	—	2 patients	—
Watanabe et al., 2011[12]	DDR identification between the two 3D MR cisternography sequences, 3D-CISS and 3D-SPACE	The DDR defined on MRI was a hypothetical boundary. Confirmation of the landmark proposed in	MRI 3D-CISS 3D-SPACE	—	10 healthy volunteers	2 radiologists	—	—	The differences in ICA visualization scores between the 3D-SPACE and 3D-CISS images

		this study was not performed in surgical cases or anatomic studies with cadaveric specimens							using Wilcoxon signed-rank sum test
Scerbak et al., 2020[13]	The position of the DDR through 4 bony landmarks: 1) the anterior clinoid-internal carotid artery intersection, 2) the optic strut, 3) the opticocarotid elevation, and 4) the base of the posterior clinoid process intradural (above the DDR plane), extradural (below the DDR plane), or transitional (the DDR plane crosses the aneurysm)	Using DDR as the main anatomic repair. Aneurysms in the carotid cave topography, in the clinoid segment (C5) of the ICA and/or transitional aneurysms would be mistakenly classified as extradural. Indirect, complex, and difficult way to deduce the DDR. Imaginary plan	CT angiography, 100 cases T2 MRA	20 cerebral hemispheres	34 IA/34 patients	2 neuroradiologists	—	27 IA/27 patients	For confidence interval calculation the Wilson score method was used
Fernandes et al., 2021[14]	The location of paraclinoid aneurysms in relation to the DDR	History of subarachnoid hemorrhage can decrease MRI accuracy using DDR as the main anatomic repair. Using DDR as the main anatomic repair. Aneurysms in the carotid cave topography, in the clinoid segment (C5) of the ICA and/or transitional aneurysms would be mistakenly classified as extradural	Coronal T2-weighted images 3T MRI with 3D fast spin echo sequence	—	25 IA/20 patients	1 neuroradiologist	—	25 IA/20 patients	The agreement between MRI and intraoperative findings were evaluated busing Cohen κ coefficient. Accuracy of MRI was calculated
Present study	The intersection between the ICA and the oculomotor nerve	Giant aneurysms can distort the anatomic structure	3T magnetic resonance imaging (MRI) and 3T MRA (coronal T2, coronal fast imaging employing steady-state acquisition, 3D TOF), sagittal T1 sequence isotropic volumetric pre and postgadolinium was added (SPACE/ spectral attenuated inversion recovery, and Cube)	20 cerebral hemispheres	42 IA/34 patients	2 neuroradiologists	42 IA/34 patients	23 IA/20 patients	A mathematical model was used excluding randomness in the concordance between the radiologic and 3D biomodel classifications. Goodman-Kruskal γ test, odds ratio, χ^2, κ index, and discordance ratio tests were used. Results confirmed with statistical relevance

IA, intracranial aneurysm; ACP, anterior clinoid process; DDR, distal dural ring; 3D- ICA, internal carotid artery; 3D, three-dimensional; CE, contrast-enhanced; MRA, magnetic resonance angiography; CT, computed tomography; CS, cavernous sinus; TOF, time of flight, CISS, constructive interference in steady state; MRI, magnetic resonance imaging; SPACE, turbo spin echo sequence sampling perfection with application-optimized contrasts using different flip angle evolution.

REFERENCES

1. Punt J. Some observations on aneurysms of the proximal internal carotid artery. *J Neurosurg*. 1979; 51:151-154.

2. Taptas JN. Intradural and extradural ICA. *J Neurosurg*. 1979;51:877-878.

3. Oikawa S, Kyoshima K, Kobayashi S. Surgical anatomy of the juxta-dural ring area. *J Neurosurg*. 1998;89:250-254.

4. Murayama Y, Sakurama K, Satoh K, Nagahiro S. Identification of the carotid artery dural ring by using three-dimensional computerized tomography angiography. Technical note. *J Neurosurg*. 2001; 95:533-536.

5. Ito K, Hongo K, Kakizawa Y, Kobayashi S. Three-dimensional contrast medium-enhanced computed tomographic cisternography for preoperative evaluation of surgical anatomy of intradural paraclinoid aneurysms of the internal carotid artery: technical note. *Neurosurgery*. 2002;51:1089-1092 [discussion 1092-1083].

6. Gonzalez LF, Walker MT, Zabramski JM, Partovi S, Wallace RC, Spetzler RF. Distinction between paraclinoid and cavernous sinus aneurysms with computed tomographic angiography. *Neurosurgery*. 2003;52:1131-1137 [discussion 1138-1139].

7. Beretta F, Sepahi AN, Zuccarello M, Tomsick TA, Keller JT. Radiographic imaging of the distal dural ring for determining the intradural or extradural location of aneurysms. *Skull Base*. 2005;15:253-261 [discussion 261-252].

8. Hashimoto K, Nozaki K, Hashimoto N. Optic strut as a radiographic landmark in evaluating neck location of a paraclinoid aneurysm. *Neurosurgery*. 2006;59:880-895 [discussion 896-897].

9. Tsuboi T, Tokunaga K, Shingo T, et al. Differentiation between intradural and extradural locations of juxta-dural ring aneurysms by using contrast-enhanced 3-dimensional time-of-flight magnetic resonance angiography. *Surg Neurol*. 2007;67: 381-387.

10. Hirai T, Kai Y, Morioka M, et al. Differentiation between paraclinoid and cavernous sinus aneurysms with contrast-enhanced 3D constructive interference in steady-state MR imaging. *AJNR Am J Neuroradiol*. 2008;29:130-133.

11. Thines L, Lee SK, Dehdashti AR, et al. Direct imaging of the distal dural ring and paraclinoid internal carotid artery aneurysms with high-resolution T2 turbo-spin echo technique at 3-T magnetic resonance imaging. *Neurosurgery*. 2009; 64:1059-1064 [discussion 1064].

12. Watanabe Y, Nakazawa T, Yamada N, et al. Identification of the distal dural ring with use of fusion images with 3D-MR cisternography and MR angiography: application to paraclinoid aneurysms. *AJNR Am J Neuroradiol*. 2009; 30:845-850.

13. Scerbak J, Lapteva O, Sahin OS, et al. Identification of the distal dural ring and definition of paraclinoid aneurysms according to bony landmarks on 3-dimensional computed tomography angiography: a cadaveric and radiological study. *Oper Neurosurg (Hagerstown)*. 2020;19: 319-329.

14. Fernandes ST, Doria-Netto HL, Alves RV, et al. The diagnostic accuracy of MRI in determining the relations between paraclinoid aneurysms and the cavernous sinus. *Neuroradiology*. 2022;64: 1175-1185.